

Harnessing Alpha Radiation to Power Miniaturized Implantable Medical Devices

Averal Kandala

Electrical Engineering and Computer Sciences
University of California, Berkeley

Technical Report No. UCB/EECS-2025-17

<http://www2.eecs.berkeley.edu/Pubs/TechRpts/2025/EECS-2025-17.html>

May 1, 2025



Copyright © 2025, by the author(s).
All rights reserved.

Permission to make digital or hard copies of all or part of this work for personal or classroom use is granted without fee provided that copies are not made or distributed for profit or commercial advantage and that copies bear this notice and the full citation on the first page. To copy otherwise, to republish, to post on servers or to redistribute to lists, requires prior specific permission.

Acknowledgement

This work was supported by the National Science Foundation Graduate Research Fellowship Program under Grant No. DGE 1752814. Any opinions, findings, and conclusions or recommendations expressed in this material are those of the author(s) and do not necessarily reflect the views of the National Science Foundation.

Harnessing Alpha Radiation to Power Miniaturized Implantable Medical Devices

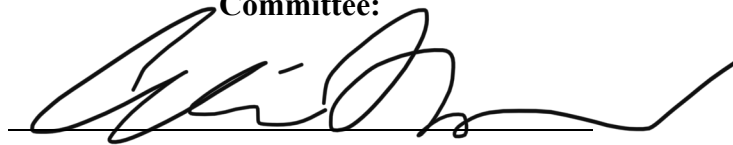
by Averal N. Kandala

Research Project

Submitted to the Department of Electrical Engineering and Computer Sciences of the University of California, Berkeley, in partial satisfaction of the requirements for the degree of **Master of Science, Plan II**.

Approval for the Report and Comprehensive Examination:

Committee:



Professor Ali M. Niknejad
Research Advisor, Chair

6/11/2021

(Date)

Mekhail Anwar

Professor M. Mekhail Anwar
Research Advisor, Co-chair

08/05/21

(Date)



Professor Robert C. N. Pilawa-Podgurski
Additional Reader

08/12/21

(Date)

Harnessing Alpha Radiation to Power Miniaturized Implantable Medical Devices

by

Averal N. Kandala

A thesis submitted in partial satisfaction of the

requirements for the degree of

Master of Science

in

Electrical Engineering and Computer Sciences

in the

Graduate Division

of the

University of California, Berkeley

Committee in charge:

Professor Ali M. Niknejad, Chair
Professor M. Mekhail Anwar, Co-chair
Professor Robert C. N. Pilawa-Podgurski

Summer 2021

Harnessing Alpha Radiation to Power Miniaturized Implantable Medical Devices

Copyright 2021
by
Averal N. Kandala

Abstract

Harnessing Alpha Radiation to Power Miniaturized Implantable Medical Devices

by

Averal N. Kandala

Master of Science in Electrical Engineering and Computer Sciences

University of California, Berkeley

Professor Ali M. Niknejad, Chair

Professor M. Mekhail Anwar, Co-chair

Implantable medical devices (IMDs) have the potential to revolutionize medical diagnostics and therapy, as they provide an avenue for care providers to receive automatic feedback on the state of the patient’s body on timescales greatly accelerated from the appointment-based paradigm of today. However, three main challenges present themselves when we consider how best to integrate IMDs with the patient’s physiology without compromising on quality of life: scalability, longevity, and convenience.

The critical factor limiting progress on all three of these frontiers is power. Although research on novel battery technologies is ongoing, commercially-available batteries simply cannot provide sufficiently long-lasting power at the scales required for most chronic diagnostic sensing applications [9, 12], and alternative “independent” power strategies either carry short lifetimes or cannot be miniaturized [41]. In the absence of a proven miniaturized independent power source, research in the last decade has focused on the development of discontinuous powering models that rely on an external device, called the “interrogator”, to beam in power for harvesting by a receiver on the implant and establish a channel for communication with the implant [7, 38, 43, 44]. Ultrasound has emerged as the most promising such model due to its low attenuation in tissue and high time-averaged intensity limit as outlined by the FDA [7, 43, 44].

However convenient this type of model might be for enabling design miniaturization, it fails in general to deliver system-level convenience from the perspective of the patient, as the interrogator typically must be optimally aligned with the implant to ensure correct operation [31]. In addition, the implant simply cannot operate when it is not receiving power from the interrogator, limiting the diagnostic applicability of these models.

In order to develop the miniaturized independent power source that would overcome these

challenges, this work presents a strategy for converting the energy of alpha radionuclides into light for harvesting by a physically surrounding photovoltaic structure. By using phosphorescent materials to achieve this conversion, optical power on the scale of hundreds of nanowatts or more can be produced in a miniature form factor across the lifetime of the radionuclide, significantly extending the applicability of the previously-abandoned “nuclear” power approach for implant energy [34]. Finally, conceptual models for system-level packaging and photovoltaic conversion and harvesting efficiency are developed, with a design methodology for an integrated power harvester and sensor hub outlined for future exploration.

This work is dedicated to the memory of Sajee Srisawas, who lost her battle with cancer less than a month ago as I write this now, midway through June of 2021. It was the privilege of a lifetime to know Sajee, and somewhere, in a now-inaccessible slice of space-time, I am still an awkward middle-school kid sitting in Sajee's kitchen, being taught the meaning of kindness, friendship, and love by her wonderful family.

Contents

Contents	ii
List of Tables	iii
List of Figures	iii
1 Introduction	1
1.1 The Need for Long-Lasting, Minimally-Invasive Wireless Implantable Medical Devices	1
1.2 Existing Approaches and State of the Art	2
1.3 Going “Nuclear”	5
1.4 Light as an Intermediate Energy Mode	8
2 Experimental Framework and Initial Investigation	10
2.1 First Hypothesis and Experiment	10
2.2 Measurement Strategy	16
2.3 QD-DOTA Experiment Results and Conclusions	21
3 Conditions for Optimal Light Generation	26
3.1 Finding the Best Phosphor	26
3.2 Optimally Combining the Radionuclide and Phosphor	28
4 Harvester Design Considerations	39
4.1 Packaging	39
4.2 Photovoltaic Structure and Characterization	40
4.3 Power Harvesting Strategies	41
4.4 Sensor Integration	49
5 Conclusion	52
5.1 Next Steps	52
5.2 Outlook	52
Bibliography	54

List of Tables

1.1	Battery comparison for 1 mJ/day sensor load.	2
1.2	General comparison of state of the art for IMD power sources.	6
3.1	Scintillating/phosphorescent materials used in second experiment.	26
3.2	Phosphor amount sweep relative activities.	36
4.1	Imaging sensor operating requirements.	49

List of Figures

1.1	Alpha light conversion IMD concept.	8
2.1	Conjugation of radionuclides to a quantum dot.	10
2.2	Th-227 decay chain.	12
2.3	Activity and emitted power over time for Th-227 sample.	13
2.4	Verification of light generation against controls.	15
2.5	Xenogen IVIS Imaging System 50 Series at UCSF.	17
2.6	Covering the LED beam angle with the power meter.	18
2.7	Imaging the LED within the IVIS using a neutral optical density filter.	19
2.8	Geometry of finding the LED beam solid angle.	20
2.9	QD-DOTA/Th-227 mixture light output compared to total emitted power	21
2.10	QD-DOTA/Th-227 mixture light output compared to Th-227 control light output	22
2.11	Evaporation and rehydration of QD-DOTA/Th-227 mixture	24
3.1	Unevaporated vial comparison.	29
3.2	Evaporated vial comparison.	30
3.3	Phosphor energy conversion efficiency comparison.	31
3.4	Phosphor and Th-227 scaling before evaporation.	32

3.5	Phosphor and Th-227 scaling after evaporation.	33
3.6	Phosphor and Th-227 scaling efficiency after evaporation.	34
4.1	Photodiode I-V curves.	42
4.2	Photodiode maximum power point.	43
4.3	Series PV connection to match the load.	44
4.4	Adaptive PV block interconnection.	45
4.5	PV power harvesting via step-up conversion.	46
4.6	PV partial power processing.	48

Acknowledgments

I would like to express my sincere gratitude to my research advisors, Professors Ali M. Niknejad and M. Mekhail Anwar, for all of the support they have provided to me thus far and will provide in the future. It is kind of hard to believe that all of this is more or less the result of a single brief conversation I had with Ali early in 2020, as well as the email I sent to Mekhail as a result of that conversation. *Carpe diem!* Or something like that, perhaps in English. Professor Robert C. N. Pilawa-Podgurski spent more time than he really needed to to help me write the fourth chapter of this, and I remain extremely grateful for that.

For all of the practical assistance they provided me, I would also like to thank the folks at UCSF's China Basin and Helen Diller facilities, including (but not necessarily limited to) Joseph Blecha, Yung-Hua Wang, Sinan Wang, Kondapa Naidu Bobba, Ryan Tang, Shalini Chopra, Ning Zhao, Zhuo Chen, Niranjana Meher, Mabel Zelaya, Celestine Fry, Byron Hann, and Paul Phojanakong. Professors Henry VanBrocklin, Youngho Seo, and Michael Evans provided invaluable advice and guidance as well.

Thank you to all of my friends in Pioneers in Engineering, especially my longtime roommate Seiya Ono, for putting up with my quirks and giving me a sense of belonging. Thanks as well to all of the friends I have made in the Anwar and Niknejad groups this year, with whom I hope to make many happy memories in the future. Special thanks to Rozhan Rabhani and Micah Roschelle for all the practical help they provided during this year, as well as the sense of community they helped me to build during these strange times.

My sincerest gratitude as well to all of the graduate student instructors (GSIs) that convinced me through their drive and passion that doing a PhD was what I really wanted to do. This list includes Efthymios Papageorgiou, David Biancolin, and Albert Magyar, among many others. Konlin Shen and Soner Sönmezoglu deserve tremendous credit for teaching me how to do research and do it well, and I would not have found a modicum of success in my graduate school and fellowship applications if Konlin had not dedicated hours upon hours to reviewing my drafts.

To all my family and friends, and especially my mother, thank you so much for the love you show me. I really would not be writing this without it. I would also like to acknowledge the financial support given to me by the State of California, which provided me with a world-class undergraduate education, as well as the National Science Foundation, which is currently providing me with a world-class graduate education to match.

This work was supported by the National Science Foundation Graduate Research Fellowship Program under Grant No. DGE 1752814. Any opinions, findings, and conclusions or recommendations expressed in this material are those of the author(s) and do not necessarily reflect the views of the National Science Foundation.

Chapter 1

Introduction

1.1 The Need for Long-Lasting, Minimally-Invasive Wireless Implantable Medical Devices

Today, most medical care is conducted in an information-limited fashion, in which a care provider applies or prescribes some treatment, and feedback on the effectiveness of that treatment reaches the care provider after some delay (or not at all), often contingent on the availability of and ease of access to diagnostic equipment. This paradigm, in which the timescale of feedback is determined directly by the logistics of using shared diagnostic instruments, is especially problematic for patients with life-threatening diseases and conditions who cannot tolerate regular travel to and from a hospital or who cannot financially afford extended stays in a hospital altogether.

One key missing link in this chain is a regular internal view into the body's physical response to treatment. External diagnostic tools are generally cumbersome and expensive and naturally bound to medical care facilities as a result. However, if the base functionalities of such tools could be imparted to a sensor that is implanted within the patient, specifically within the region of the body undergoing treatment, and can transmit data to the care provider, the care feedback loop would be greatly accelerated and the patient's quality of care (and life) would improve dramatically accordingly.

Systems that satisfy this description, as well as those that have some treatment capabilities themselves, are referred to as implantable medical devices (IMDs). To integrate these devices well within the patient's body and lifestyle, an IMD designer must address three salient issues: scalability, longevity, and convenience.

The need for scalability arises from the fact that larger structures are simply less welcome in the body environment: larger implant sizes result in greater tissue response and can also lead to greater patient discomfort [53]. The catch-all phrase used to describe this phenomenon is "invasivity", and research has identified that implants on the order of millimeters (mm), specifically those of the form factor of fiducial markers used in radiation therapy (1 mm \times 1 mm \times 5 mm), are sufficiently minimally-invasive to allow for their safe integration

into the body over clinical timescales (months to years) [13, 22].

In addition, wireless systems are preferable in general to wired systems, as wired devices can introduce the possibility of infection. Moreover, wired systems are also susceptible to chronic degradation and can induce tissue damage that can limit their operation [17]. To ensure that the patient is not forced to regularly operate complicated equipment to extract sensor data or power their implant(s), the ideal IMD should allow for convenient (minimal) operation. In addition to providing utility over a larger range of applications, a long-lasting implant system, especially one which can power itself or otherwise derive power without external action, goes a long way toward achieving this higher-level goal of maximal convenience. Powering and communication strategies for achieving this type of long-lasting IMD are described in the next section.

1.2 Existing Approaches and State of the Art

Batteries

A natural first candidate for powering just about any electronic device is the battery. Batteries offer high energy density, as well as safe and robust operation [41]. Indeed, lithium batteries have found use in cardiac pacemakers and other chronically implanted devices for decades now, reliably providing power for up to 10 years [41]. However, as might be expected, the energy storage capacity of any battery design is tied closely to its size, with smaller batteries of a given technology offering generally lower energy storage capacity. As a result, without an associated apparatus to harvest energy and re-charge an implant's battery, the lifetime of the system is limited directly by the amount of energy the battery holds upon implantation, its self-discharge characteristics, and the voltage and power requirements of the implant system.

Table 1.1: Battery comparison for 1 mJ/day sensor load.

Battery	Chemical System	Size	Voltage	Capacity
Cymbet CBC005 [9]	Li-ion	1.7 mm × 2.2 mm × 0.20 mm	3 to 4.2 V	5 μAh
Front Edge NanoEnergy®[12]	Li-ion	20 mm × 25 mm × 0.3 mm	3.8 to 4.2 V	1 mAh
Masurkar et al. [27]	Li-ion	3 mm × 3 mm × 0.5 mm	3.2 to 3.6 V	35 μAh
Yin et al. [61, 68]	AgO-Zn	10 mm × 10 mm × ~0.8 mm	~1.55 V	~8 mAh

Battery	$E[0]$	Energy Density	Z_{int}	Self-Discharge	Lifetime
Cymbet CBC005 [9]	64.8 mJ	0.087 J/mm ³	7000 to 30000 Ω	1.5% per year	64 days
Front Edge NanoEnergy®[12]	14.4 J	0.096 J/mm ³	-	<5% per year	4844 days
Masurkar et al. [27]	428 mJ	0.095 J/mm ³	1750 Ω	-	<428 days
Yin et al. [61, 68]	44.64 J	0.558 J/mm ³	~5 Ω	3% per month	991 days

Table 1.1 summarizes the expected lifetime and size of a number of state-of-the-art and commercially-available batteries potentially applicable to IMDs when tasked with powering a sensor requiring 1 mJ of energy on a daily basis, without recharging and at room temperature. The battery lifetime is estimated according to the following calculation, in which V_{mid} is the average operating voltage of the battery across a discharge cycle and estimated minimum voltage expected by the load, $E[n]$ is the useful energy (with respect to the limit imposed by V_{mid}) stored by the battery on day n , C_d is the discharged (current) capacity of the battery in Ah at V_{mid} , D_{self} is the fractional self-discharge per day, and E_{sensor} is the energy required by the sensor per day (1 mJ in the presented scenario):

$$E[0] = V_{mid}C_d \quad (1.1)$$

$$E[n] = E[0] - n(D_{self}E[0] + E_{sensor}) \quad (1.2)$$

$$n_{lifetime} < \frac{E[0]}{D_{self}E[0] + E_{sensor}} = \frac{1}{D_{self} + \frac{E_{sensor}}{E[0]}} \quad (1.3)$$

Note that, due to the internal impedance and inherent current limitations of each battery, an additional “boosting” capacitor is generally required for lower capacity designs to achieve the desired peak current at the load (on the order of mA). In addition, heightened temperatures within the body should cause self-discharge to exceed values reported at room temperature, decreasing the expected lifetime from the approximated values in implanted conditions.

From this analysis, it is clear that the research state of the art is moving quickly toward enabling highly dense, long-lasting battery power at mm-scale, with direct medical implant applicability following naturally as a result. It is not unreasonable to expect that a battery storing 1 J in a 1 mm³ form factor could be presented in the near future, although it is not clear whether the self-discharge characteristics of such a battery would allow it to have a useful lifetime of any longer than a year. Indeed, self-discharge is a primary limiter of current battery implementations: straightforwardly applying the uniform areal capacity scaling presented in [61] to that highly energy-dense design would project that a similar battery with a cross-sectional area of 1 mm² should have a lifetime of only around 10 days for the 1 mJ sensor application explored above. Certainly, this would pose significant challenges for integrating batteries like this into IMD systems without built-in recharging mechanisms. In addition, miniaturization and maintaining high energy density following miniaturization remain non-trivial obstacles to overcome. 3D printing technologies offer a promising path forward on this front [27, 61].

Since a long-lasting, sufficiently-miniature battery has not yet been demonstrated, research has proceeded in the meantime on alternative strategies for powering minimally-invasive IMDs. The innovative concept which underlines most “cutting-edge” research in this field today is that of wireless power, in which the implant power source is replaced by a transducer for converting energy beamed into the body from outside.

Electromagnetics

Just as the battery is the natural first candidate for a continuous power source on the implant itself, electromagnetic (EM) waves seem to be a convenient option for achieving wireless power, as the literature on antennas and EM wave propagation for radio-frequency (RF) communication is well-established. The potential for the multiplexing of the implant antenna as a means of receiving power from and communicating with an external device, termed the “interrogator” based on the similar setup of radio-frequency identification (RFID) systems, is especially appealing. However, EM power transfer through the body is exceedingly lossy in general, with performance degrading significantly for antenna sizes below $4 \times 4 \text{ mm}^2$ [38, 44]. Furthermore, a host of other issues arise in any scheme making use of EM power transmission, including losses in matching networks due to the low quality factors of on-chip capacitors and inductors, as well as potential excessive heating of neighboring tissue due to the inability to sufficiently focus relatively long wavelength EM waves, among others [7].

Ultrasound

Ultrasound (US) has emerged as the preferred strategy for achieving wireless power and communication through the body due to its significantly lower path loss through tissue compared to EM [44]. In addition, the small wavelength of acoustic waves places the theoretical minimum size of the implant US transducer for reasonable power transfer efficiency on the order of $100 \times 100 \times 100 \mu\text{m}^3$, making US power transfer far more suitable from a system level for miniaturized IMDs [43]. In practice, the combined implant US transducer and transceiver is implemented as a piezoelectric crystal with electrical connections to a full-wave rectifier for AC-DC power conversion and field-effect transistor (FET) for “backscatter” uplink data transmission, with the interrogator modulating the US beam to send basic downlink commands [31, 49]. The backscatter communication strategy is carried over from RFID design and involves the exploitation of the dependence of the acoustic reflectivity of the piezoelectric crystal on its electrical load. The transmitter FET, placed across the terminals of the piezoelectric crystal, directly sets the load through its drain-to-source impedance, which is digitally modulated by the implant application-specific integrated circuit (ASIC) through the voltage at the gate [43]. This allows the implant to reflect incident acoustic waves such that they vary in discrete levels, enabling digital communication from the implant to the interrogator.

Alternatives

While this wireless approach allows for the combination of power and communication as described above, it inherently limits the target implant to discontinuous operation in the absence of a supplementary energy storage source, such as a battery, beyond the necessary antenna or transducer. Indeed, some argue that the ideal wireless implant system should be free altogether of the energy storage problems associated with batteries and large capacitors

[43], necessitating regular interrogation of the implant in order to collect and retrieve data. This design decision trades off convenience in operation for increased implant compactness and system longevity unlimited by any power source. However, the additional challenges introduced in this trade-off extend beyond placing the onus of operating interrogator equipment and collecting timely data on the patient or the immediate caregivers of the patient. For US-based systems especially, minute external translational (\sim mm) and angular (\sim 30°) misalignments of the external interrogator can result in insufficient energy being harvested by the implant, preventing successful operation [31]. Over long timescales, this can prove to be a significant impediment to both the acquisition of meaningful diagnostic data and the patient’s lifestyle.

While the research community has been particularly excited by the potential of wireless power strategies over the last decade, a good deal of effort continues to be devoted to the development of continuous on-chip power sources to directly replace or augment the capabilities of batteries within implants. One particularly promising candidate for such a power source is the glucose biofuel cell, which harnesses the abundance of glucose and oxygen found within the mammalian body and has been demonstrated to power electrical circuits when implanted within a rat [41, 65]. There are, however, a number of significant obstacles to overcome before glucose biofuel cells can reliably be deployed to power minimally-invasive IMDs. These obstacles include potential enzyme instability, which can limit cell lifetime, miniaturization beyond cm-scale, and packaging for long-term biocompatibility and in vivo operation [20, 41, 66]. Additional approaches to “scavenge” energy from various sources within the body have been proposed as well, including piezoelectric [11, 67], thermoelectric [60], electrostatic [1], and electromagnetic methods [69], but these strategies are limited to specific bodily contexts (e.g., those involving significant movement or temperature gradients) and generally have not yet been demonstrated at mm-scale.

Another concept that has been implemented to successfully power long-lasting IMDs in the past is that of harvesting the energy present in certain alpha and beta radionuclides. This so-called “nuclear battery” approach, applied safely in cardiac pacemakers, fell out of vogue as lithium battery technology became more robust and reliable in the 1980s [34]. Key challenges to the numerous variations on this approach include packaging and miniaturization, as well as system-level robustness and longevity, and will be explored more thoroughly in the next section. Table 1.2, below, summarizes the benefits and limitations of the most promising existing IMD power strategies described in this section and the next.

1.3 Going “Nuclear”

As mentioned briefly in the previous section, serious exploration of the “nuclear battery” concept in the 1970s and 1980s resulted in the successful deployment of a variety of these devices to power cardiac pacemakers during this period, with statistically-estimated failure rates below 0.1% overall and at least one model, the Coratomic nuclear battery, exhibiting no failures across 27000 unit months [34]. In this section, we will explore the core technology

Table 1.2: General comparison of state of the art for IMD power sources.

Power Source	Potential for Lifetime >1 year with 1 mJ/day Sensor?	Miniaturizable	Packaging/Bio-compatibility Concerns?	Environment Independent?	Wireless/Requires Interrogator?	Demonstrated in vivo?
Rechargeable Battery [27, 61]	Yes	Yes	No	Yes	No	Yes
Glucose Biofuel Cell [26, 38, 65, 66]	Depends on catalyst lifetime	Yes	Yes	No	No	Yes
Radioisotope Thermoelectric Generator [34, 56, 63]	Yes	No	No	Yes	No	Yes
Alphavoltaic [4, 23, 42, 50]	No	Yes	No	Yes	No	No
Betavoltaic [34, 50]	Yes	Depends on stack and package size	Yes	Yes	No	Yes
Ultrasound [31, 43]	Yes	Yes	No	Yes	Yes	Yes
Electromagnetics [7, 16, 38, 44]	Yes	Depends on depth and antenna size	Depends on beamed power	Depends on depth	Yes	Yes

behind these devices and investigate how the fundamental concepts from this analysis could inform the design of a more modern radionuclide-based power source for IMDs.

RTGs

The devices described above are known more precisely as radioisotope thermoelectric generators (RTGs), and, at a basic level, each such device uses a radioisotope (also called a “radionuclide”), typically an emitter of alpha or beta particles, as a heat source to produce electricity through a thermoelectric generator. The primary concern regarding this power scheme might be its safety; however, alpha particles can be shielded by any relatively thin physical enclosure and beta particles can be shielded with a thicker layer of glass or metal [33]. Alpha and beta radionuclides (and the interaction of beta particles with their shields) can both produce more dangerous ionizing radiation, such as gamma or X-ray radiation [46], but the total radiation dose experienced by patients with implanted nuclear-powered cardiac pacemakers was negligible (e.g., less than that felt by regular inhabitants of Denver, Colorado) [34]. Furthermore, the thermoelectric method of energy conversion is relatively robust, enabling reliable energy conversion over many years. In fact, when used in conjunction with radioisotopes with sufficiently long half-lives, pacemakers operating with RTG-based nuclear batteries frequently outlasted their host patients, necessitating the introduction of measures to track and collect these devices [34].

Although thermoelectric energy conversion is not particularly efficient — state-of-the-art RTG energy conversion efficiency is around 1% [56] — RTGs can be miniaturized to cm-scale form factors, which made them an attractive choice for pacemakers when lithium battery technology was not fully developed. Unfortunately, the miniaturizability of thermoelectric generators does not seem to extend to mm-scales, as the useful power output of each RTG device corresponds directly to the size of the heat source [63]. Each RTG requires sufficient insulation to prevent heat loss to the surrounding biosphere, compounding the difficulty of miniaturizing these devices [34]. Furthermore, common radionuclides used in these first nuclear batteries, such as plutonium-238, have been difficult to procure over the last few

decades, with federal production beginning to ramp up again only very recently for deep space applications [29, 55]. Taken together, these realities suggest that RTG technology is not a good choice for powering mm-scale IMDs, with the need for further miniaturization posing the greatest challenge. Indeed, given these practical issues, it makes sense that batteries have long since eclipsed RTGs as the preferred power sources for cardiac pacemakers [34, 41].

Practical considerations aside, radionuclide-based power sources are an attractive prospect simply because the radionuclides themselves hold an incredibly large amount of energy. As an example, the power density of the plutonium-238 used in cardiac pacemakers was reported to be 3.9 W/cm^3 [34]. Conservatively assuming single exponential decay with a half-life of 87.8 years, and thereby disregarding the radioactivity of daughter radionuclides, the total integrated energy available from 1 mm^3 of plutonium-238 therefore exceeds 10.8 million joules [34]! Clearly, any method of reliably converting even a fraction of this energy into useful electrical power would enable incredibly long-lasting IMDs and high-power sensing, potentially far outstripping the capabilities of even the best batteries developed in the future.

Alphavoltaics

Since alpha radiation is the easiest to shield, alphavoltaic energy conversion, in which a semiconductor converts incident alpha particles directly into electrical current, can theoretically allow for an extremely miniature power source with far greater conversion efficiency than is achievable through simple thermoelectric conversion [23, 42, 56]. The caveat to this assertion is the unfortunate fact that these direct alphavoltaics experience severe degradation through radiation damage of the semiconductor [4, 23, 42], with the useful lifetime of such a system reduced to less than a month [42]. As an additional limiting consideration, the alpha source for any alphavoltaic device must be applied in a very thin layer (tens of microns) atop the semiconductor to avoid absorption in the intermediate medium (e.g., air) or self-absorption due to the extremely limited range of alpha particles in most materials [50]. It is this phenomenon, in fact, which makes these particles so easy to shield.

Betavoltaics

Betavoltaic devices, which are functionally the same as alphavoltaics but derive power from beta radiation rather than alpha radiation, offer a more straightforward path to achieving long-lasting power through direct conversion of radiation. Although beta particles generally can cause semiconductor radiation damage as well, this damage can be minimized, especially through the use of a relatively low energy radionuclide such as tritium (hydrogen-3) [23, 50]. However, self-absorption limits the useful thickness of any beta-emitting radionuclide to just a few microns, necessitating sandwiched stacks of semiconductor and radioisotope layers to achieve reasonable power output [50]. Altogether, the need to add additional shielding to protect the body beyond a simple enclosure, combined with significant availability and cost

issues and the stacking requirement, means that quite a bit more work is required to design betavoltaic power sources suitable for mm-scale IMDs [33, 46, 50].

Selecting a Strategy

Finally, radioisotope-based thermophotovoltaic (RTPV) energy conversion is an interesting alternative to conventional thermoelectric conversion that can be applied for similar fuel sources, such as plutonium-238 [10]. However, a preliminary review of the literature on thermophotovoltaic conversion did not indicate that efforts are being made to miniaturize RTPV devices beyond the cm-scale. Indeed, just as with an RTG, an RTPV system would require significant insulation to operate safely within the body, as operating temperatures typically exceed 1000 K [10].

The challenges facing radiation-based power sources potentially applicable to mm-scale IMDs center overwhelmingly around miniaturization and longevity. In order to enable miniaturization, a relatively low temperature, alpha-emitting radioisotope source is desired, to ensure that the packaging and enclosure of the device does not determine its minimum size. To ensure implant longevity, the energy conversion method should be robust to radiation damage, either through the inherent isolation of the converting mechanism from the radiation or the use of a radiation-resistant substrate. In the next section, the former strategy for longevity is explored, with a view to overcoming the issues that plague direct alphavoltaics.

1.4 Light as an Intermediate Energy Mode

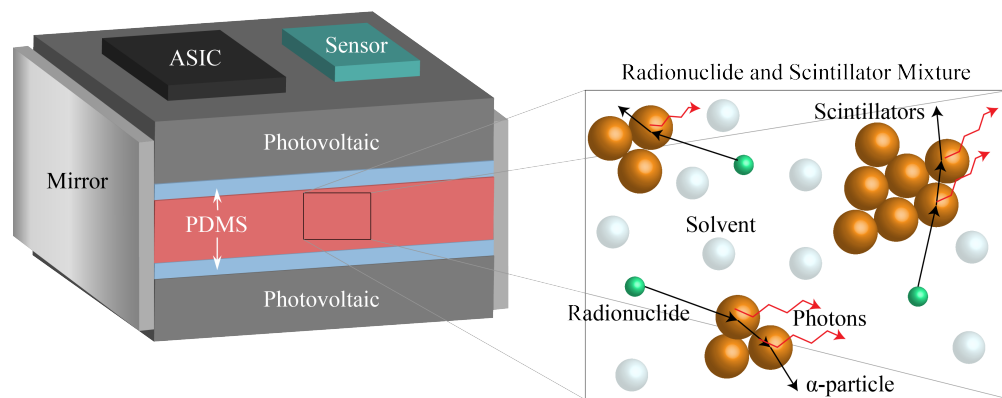


Figure 1.1: Conceptual illustration of proposed concept integrated with an IMD. The material labeled as a scintillator could also be a phosphor.

In order to improve upon the conversion efficiency of direct alphavoltaics, an indirect energy conversion method has been suggested in [23], in which an intermediate material absorbs the incident radiation and emits light which can generate electron-hole pairs within

the semiconductor (this is the concept behind photovoltaic devices), thereby completing the conversion to electrical energy. This intermediate conversion to light can significantly augment the overall energy conversion efficiency of the system, with the selection of the light-emitting material (a phosphor or scintillator) playing a key role [23]. A scintillating material can potentially be integrated into the semiconductor itself [4, 18, 23]; however, this indirect conversion strategy is particularly attractive to begin with because it allows the (α) radiation source to be isolated from the semiconductor by an optically clear material, which in almost every case will be capable of protecting the semiconductor from radiation damage. Therefore, through this simple modification of the conventional alphavoltaic structure, system longevity on the order of multiple source half-lives can be achieved, at a scale limited solely by the power requirements of the IMD and the capabilities of microfabrication and chemical deposition processes. Demonstration of the feasibility of this concept is the primary focus of the remainder of this work, with additional system- and circuit-level design considerations described to enable eventual construction of a system similar to the one illustrated in Figure 1.1.

Chapter 2

Experimental Framework and Initial Investigation

2.1 First Hypothesis and Experiment

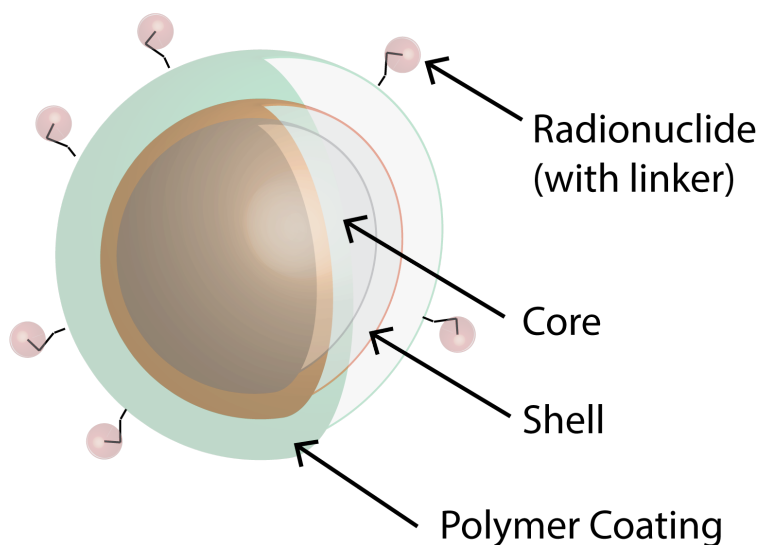


Figure 2.1: Conceptual diagram of chemical conjugation/chelation of radionuclides to a quantum dot.

Chemical Conjugation

Given the preponderance of articles in the literature suggesting that quantum dots (QDs) are good candidates for scintillating radiation detection and boosters of semiconductor radiation-to-electrical energy conversion efficiency in alphavoltaic and betavoltaic systems [4, 8, 18, 21,

23, 24, 25], our initial investigation centered around evaluating a method of improving QD scintillation through chemical conjugation of QDs to radionuclides in solution. This strategy was hypothesized to facilitate the improvement of scintillation efficiency by fixing multiple smaller radionuclides around each larger QD (sized on the order of tens of nm) through the chelating agent. Since the radionuclides ideally would not be free-floating in the solution after this conjugation/chelation process, the average distance between each radionuclide and the nearest QD, which would be the one the radionuclide would be conjugated to, could potentially be lower. This would improve the system scintillation efficiency by minimizing the energy deposited by emitted alpha particles in the solvent and maximizing the energy deposited within the relatively high quantum yield ($\geq 50\%$) QDs instead [36], allowing for more light to be generated overall. The distance between the alpha emitter and the scintillator in this sort of system is especially important because of the extremely small stopping range of alpha particles in liquid solution, which is typically on the order of tens of microns[6]. In addition, this structure would ideally enforce a more thorough dispersion of the radionuclide within the solution, avoiding the scenario in which the scintillating material and the radionuclide form distinct layers, which can create a shielding effect.

Alpha Radionuclide and Decay Analysis

The alpha radionuclide selected for use in our experiments was thorium-227 (Th-227), which can be procured via secure shipment from Oak Ridge National Laboratory (ORNL) in Tennessee. Th-227 was a convenient and relevant choice for a number of reasons. First, Th-227 and its daughter radionuclides emit beta and gamma radiation at a negligible level, obviating any need for significant shielding [28]. In addition, Th-227 has a half-life of 18.7 days [28], which is quite long for radiolabeling purposes in the biomedical imaging field, but seems relatively short compared to the eventual desired lifetime of an ideal IMD (months to years). However, the first alpha decay product of Th-227 is Ra-223, which is another alpha emitter with a half-life of 11.4 days [28]. In addition, as can be seen in Figure 2.2, after Ra-223 decays to Rn-219, Rn-219 undergoes five additional decays in quick succession, meaning that, effectively, there are six total decays for each real Ra-223 decay. The total radioactivity (“activity”), or number of decays per second, of any given sample of initially pure Th-227 therefore evolves approximately according to the following calculation, in which A represents activity, N represents the amount (in nuclei) of a certain radionuclide, λ represents decay rate, and $T_{1/2}$ represents half-life [3].

Writing the decay equations:

$$\lambda = \frac{\ln(2)}{T_{1/2}} \quad (2.1)$$

$$A_{Th} = -\frac{dN_{Th}}{dt} = \lambda_{Th}N_{Th} \quad (2.2)$$

$$\frac{dN_{Ra}}{dt} = -\lambda_{Ra}N_{Ra} + \lambda_{Th}N_{Th} \text{ and } A_{Ra} \approx 6\lambda_{Ra}N_{Ra} \quad (2.3)$$

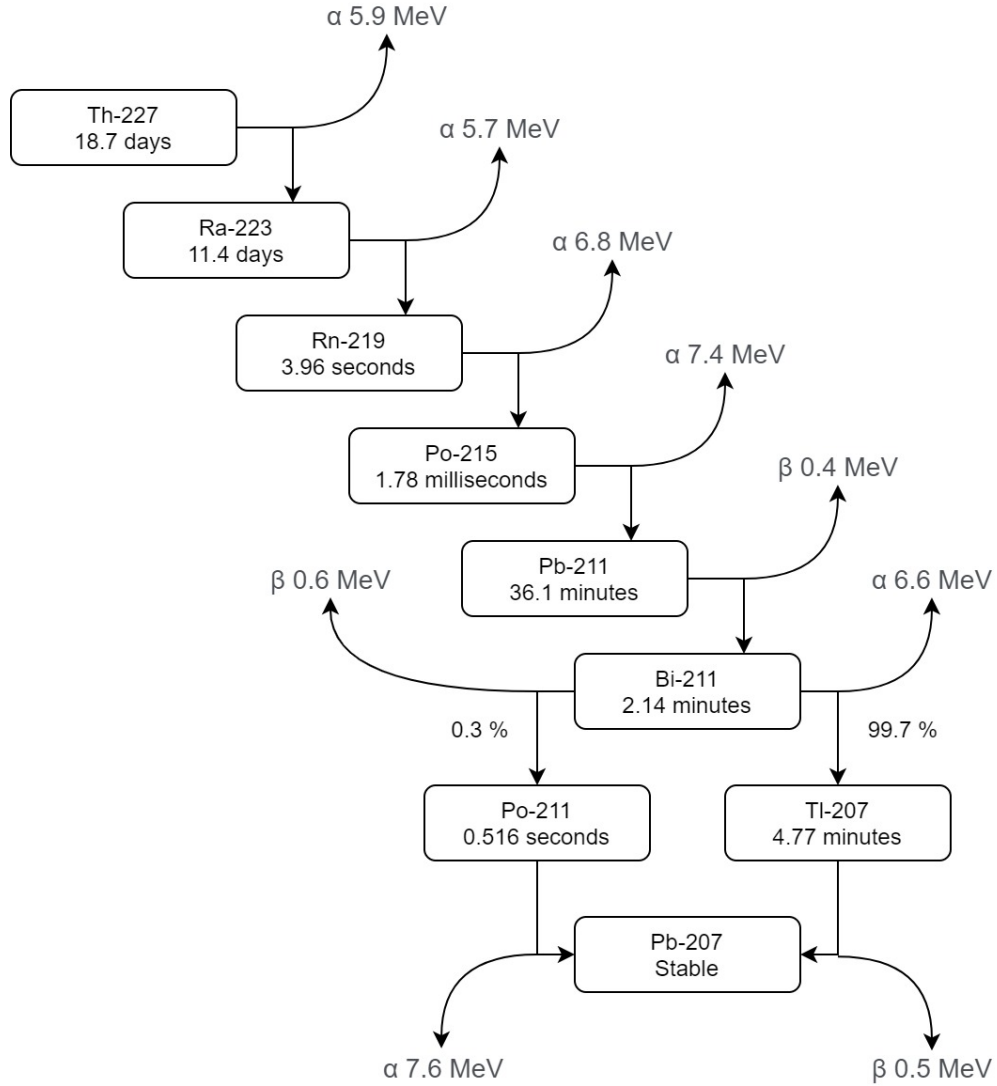


Figure 2.2: Th-227 decay chain, adapted from [15].

The solutions to these differential equations are the following:

$$N_{Th} = N_{Th,0}e^{-\lambda_{Th}t}, \quad A_{Th} = A_{Th,0}e^{-\lambda_{Th}t} \quad (2.4)$$

and

$$N_{Ra} = \frac{\lambda_{Th}}{\lambda_{Ra} - \lambda_{Th}} N_{Th,0}(e^{-\lambda_{Th}t} - e^{-\lambda_{Ra}t}) + N_{Ra,0}e^{-\lambda_{Ra}t} \quad (2.5)$$

with no daughter activity initially ($A_{Ra,0} = \lambda_{Ra}N_{Ra,0} = 0$) implying that

$$A_{Ra} \approx \frac{6\lambda_{Ra}}{\lambda_{Ra} - \lambda_{Th}} A_{Th,0}(e^{-\lambda_{Th}t} - e^{-\lambda_{Ra}t}) \quad (2.6)$$

and, finally,

$$A_{tot} \approx A_{Th} + A_{Ra} \approx A_{Th,0} \left(e^{-\lambda_{Th}t} + \frac{6\lambda_{Ra}}{\lambda_{Ra} - \lambda_{Th}} (e^{-\lambda_{Th}t} - e^{-\lambda_{Ra}t}) \right) \quad (2.7)$$

In this specific case, Th-227 and Ra-223 are in “transient equilibrium” [3], where the production of Ra-223 actually causes the total activity to increase initially. This is a practically very useful phenomenon, as it ensures that the period in which the Th-227 fuel source is providing the most power does not begin immediately following production (e.g., at ORNL), allowing time for the fuel to be shipped and then integrated within an IMD before implantation. This is depicted in Figure 2.3, for an initial activity of 75 μCi (where 1 Ci is equivalent to 3.7×10^{10} decays per second), which proved to be a convenient unit for the purposes of these experiments.

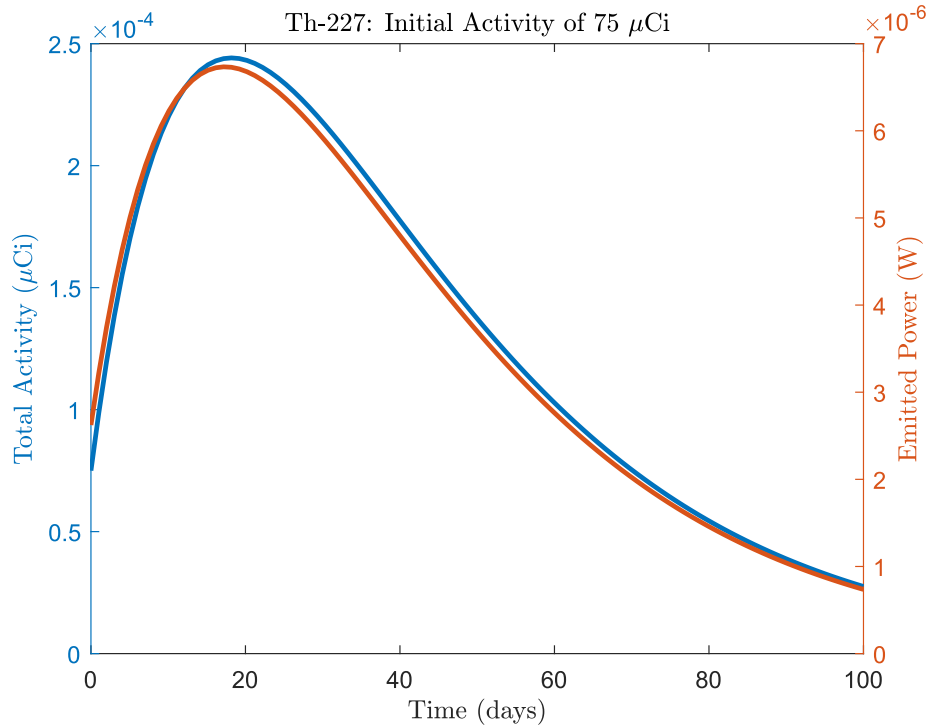


Figure 2.3: Activity (initially lower) and emitted power (initially higher) of a Th-227 sample with an initial activity of 75 μCi over time, including delay products following Ra-223 as decaying simultaneously with their Ra-223 parent. The time axis is marked in terms of days following production.

Furthermore, the high energies of the alpha emissions from Th-227 (5.9 MeV [15]) and its daughter nuclides allow even a minuscule sample of Th-227 to produce a tremendous amount of power over its lifetime. Across the decays that occur in quick succession after the decay

from Ra-223 to Rn-219, three are guaranteed to result in high energy alpha emissions, with beta emissions being comparatively negligible. This increases the average effective alpha emission energy of each Ra-223 decay from 5.7 MeV to 26.5 MeV! As a result, the emitted power as a function of time can be expressed as

$$P(t) \approx A_{Th,0}(5.9 \text{ MeV} \cdot e^{-\lambda_{Th}t} + 26.5 \text{ MeV} \cdot \frac{\lambda_{Ra}}{\lambda_{Ra} - \lambda_{Th}}(e^{-\lambda_{Th}t} - e^{-\lambda_{Ra}t})). \quad (2.8)$$

ORNL provides Th-227 in a nitrate form with a specific activity of 3.073×10^4 Ci/g at production. The density of thorium nitrate is 2.80 g/cm^3 [14], implying through dimensional analysis that a sample with an initial activity of $75 \text{ } \mu\text{Ci}$ occupies a volume of only $8.716 \times 10^{-7} \text{ mm}^3$! Inspecting Figure 2.3 once more, the maximum power produced by such a sample is around $2.8 \text{ } \mu\text{W}$. At this point in time, the power density of any sample of Th-227 is therefore 3.212 W/mm^3 , and the power density remains on the order of 1 W/mm^3 for close to two months. Given that the requisite useful power density needed to operate a 1 mJ sensor on a daily basis is around 10 nW/mm^3 (assuming lossless energy storage), Th-227, as well as alpha radionuclides like it, clearly has tremendous potential for powering mm-scale IMDs.

Experiment

Working in conjunction with researchers in the Department of Radiology & Biomedical Imaging at the University of California, San Francisco (UCSF), a sample of Th-227 was procured from ORNL and dissolved in 0.2 M HCl (hydrochloric acid) for distribution. $14 \text{ } \mu\text{L}$ of this radionuclide solution was then added in a plastic centrifuge tube (referred to here as a “vial”) to $200 \text{ } \mu\text{L}$ of phosphate buffered saline (PBS) solution containing 160 pmol of CdSSe/ZnS core/shell quantum dots (Ocean NanoTech [36]) at a concentration of $0.8 \text{ } \mu\text{M}$, previously conjugated to the organic chelator DOTA (also known as tetraxetan). Due to logistical delays, this combined solution was only prepared in time for measurements to begin on the 16th day following Th-227 production. The activity of this vial at that point was measured empirically to be about $37.5 \text{ } \mu\text{Ci}$, with an additional control vial containing $200 \text{ } \mu\text{L}$ of diluted Th-227 HCl solution measured to have an activity of around $20 \text{ } \mu\text{Ci}$ on the same day. Based on these figures, initial activities for both vials can be calculated.

$$37.5 \text{ } \mu\text{Ci} \approx A_{QD,0}(e^{-\lambda_{Th}t_1} + \frac{6\lambda_{Ra}}{\lambda_{Ra} - \lambda_{Th}}(e^{-\lambda_{Th}t_1} - e^{-\lambda_{Ra}t_1})) \quad (2.9)$$

$$20 \text{ } \mu\text{Ci} \approx A_{control,0}(e^{-\lambda_{Th}t_1} + \frac{6\lambda_{Ra}}{\lambda_{Ra} - \lambda_{Th}}(e^{-\lambda_{Th}t_1} - e^{-\lambda_{Ra}t_1})) \quad (2.10)$$

For $t_1 = 16$ days, we arrive at $11.6 \text{ } \mu\text{Ci}$ as the initial activity for the QD-DOTA/Th-227 mixture and $6.2 \text{ } \mu\text{Ci}$ as the initial activity for the control vial, with the significant discrepancy for each arising due to the large initial rise in activity that comes about due to the rapid succession of decays that follows the decay of Ra-223. However, because the

(gamma) radiation counting mechanism used was not correctly calibrated for Th-227 or its daughter nuclides, these activity values are approximate at best. In addition, the product of the QD-DOTA conjugation was not empirically characterized. These issues and their ramifications are discussed in Section 2.3.

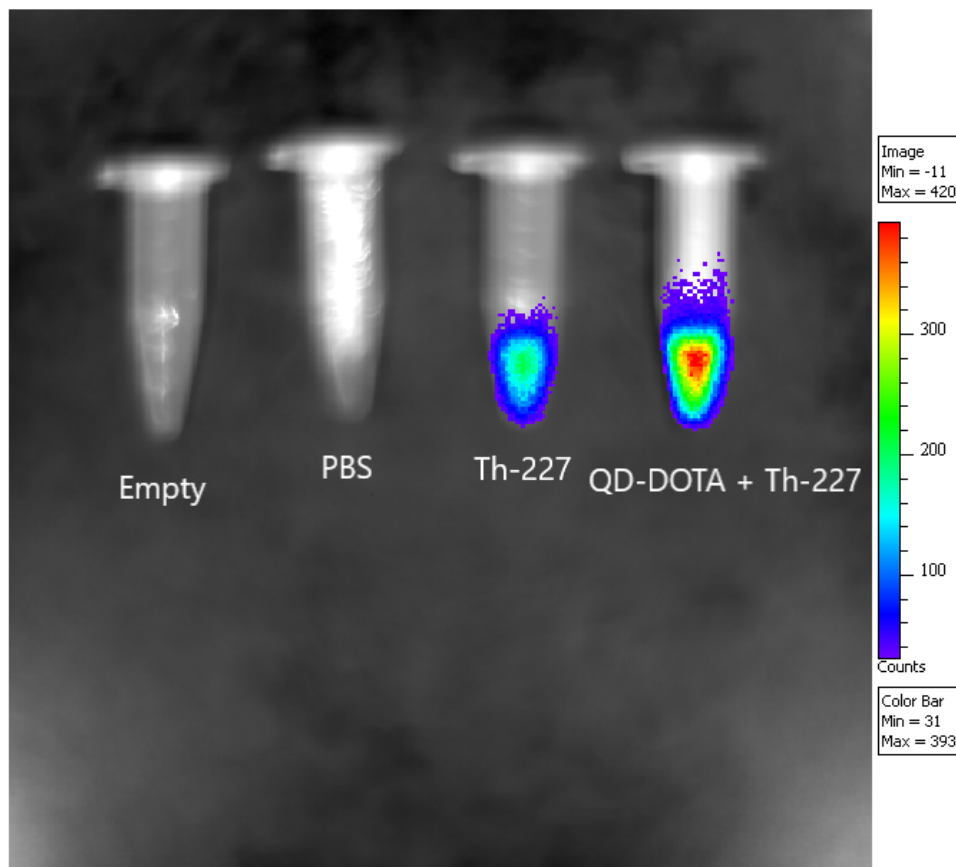


Figure 2.4: Comparison of light output from vial containing mixture of QD-DOTA with Th-227 with three negative controls. From left to right: an empty vial, a vial containing only PBS, a vial only containing 200 μL of diluted Th-227 HCl solution with a measured activity around 20 μCi on the first day of measurement, and the relevant vial containing the mixed solution of QD-DOTA and Th-227 in a volume of 214 μCi and with a measured activity around 37.5 μCi on the first day of measurement.

Despite its irregularities, this first experiment *did* succeed in establishing that this sort of radionuclide-scintillator mixture can produce a quantifiable amount of light at a level greater than the “single photon” level expected in most typical scintillation radiation counting applications [54]. Included in Figure 2.4 is an image depicting the light output from one vial containing the described QD-DOTA and Th-227 mixture compared to the light output of three negative control vials beside it: one only containing 200 μL of diluted Th-227 HCl

solution as described before, one only containing PBS, and one completely empty. As can be seen in this image, no light appears to be emitted from the empty vial and the vial containing only PBS, as would be expected. The vial of interest appears to emit noticeably more light than its neighbors, although the vial containing only the Th-227 solution produces light as well, likely due to Cherenkov radiation resulting from the transit of beta particles emitted by Th-227 decay products through the liquid solution [57]. A broad description of the imaging setup used to acquire this image, as well as a specific strategy for mapping the “counts” shown here to optical power values, is provided in the next section, with a more in-depth discussion of the experiment results in Section 2.3.

2.2 Measurement Strategy

Imaging System

A Xenogen IVIS Imaging System 50 Series (“IVIS”) machine at UCSF was used to acquire the image shown in Figure 2.4, as well as the remainder of the precise imaging data presented in this work. The charge-coupling device (CCD) camera of the IVIS is rated to have exceedingly low read noise and $\sim 85\%$ quantum efficiency for light wavelengths between 400 and 700 nm, with this rating dropping to above 50% for all wavelengths between 350 and 900 nm [19]. These properties allow the light-emitting vials in Figure 2.4 and many other images like it to be differentiated relatively accurately, given that the emission spectrum of the QDs used peaks at 645 nm. However, the values assigned to the pixels of each image produced by this system (“counts”) have no nominal conversion to units of optical power specified beyond an undefined proportional relationship with the number of photons incident on the pixels during exposure. As a result, considerable effort was required to perform a relatively accurately calibration of the measurements from the IVIS to an optical power reference.

Calibration

This calibration was achieved mainly through the use of a simple light-emitting diode (LED) circuit, combined with an optical power meter. To form the circuit, a resistor was placed in series with a 5 V DC source and the LED so as to limit current and set the output optical power. The light from the LED was then measured through the optical power meter within a light-tight box. Finally, the LED was imaged within the IVIS, with a neutral density filter of known transmission covering the LED to avoid camera pixel saturation. This filter was necessary during this calibration process (and not often afterward) because even the lowest power values that could be read through the optical power meter (tens of nW) would result in image saturation due to the relatively focused nature of the LED light beam. With values in IVIS “counts” and optical power established for the same light source, a mapping between the two can be found in general according to the derivation that follows. Note that “total counts” values arise from the summation of all of the pixel counts in the region of interest



(a) IVIS interior.



(b) IVIS control and computing setup.

Figure 2.5: Xenogen IVIS Imaging System 50 Series at UCSF.

(ROI) of any given image, minus the corresponding background noise values. For example, in the case that multiple subjects are present in the same image, summation would only occur for the pixels representing the subject in question. For images containing only one subject, the summation is done over the entire image, with any extra counts arising from extraneous pixels generally being negligible. The lower CCD quantum efficiency outside of the 400 to 700 nm wavelength range is discussed as a relevant consideration in the next chapter.

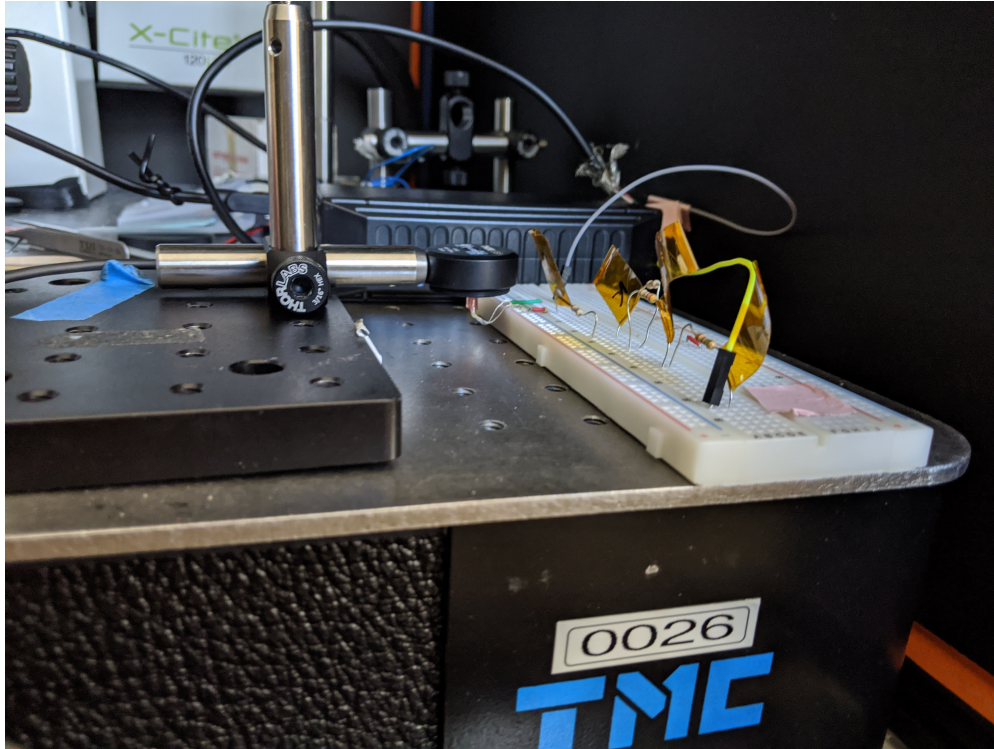


Figure 2.6: Covering the LED beam angle with the power meter.

First, there is the matter of accounting for the fact that the LED has a limited viewing (beam) angle, while the subject (a vial emitting light) emits light uniformly across all 4π steradians.

$$\frac{\text{Imaged Subject Counts}}{\text{Total Subject Counts}} = \frac{\text{IVIS Imaging Solid Angle}}{4\pi} \quad (2.11)$$

$$\frac{\text{Imaged LED Counts}}{\text{Total LED Counts}} = \frac{\text{Filter Attenuation} \cdot \text{IVIS Imaging Solid Angle}}{\text{LED Beam Solid Angle}} \quad (2.12)$$

$$\frac{\text{Total Subject Power}}{\text{Total LED Power}} = \frac{\text{Total Subject Counts/Subject Exposure Time}}{\text{Total LED Counts/LED Exposure Time}} \quad (2.13)$$

$$\text{Letting } N = \frac{\text{LED Exposure Time}}{\text{Subject Exposure Time}}, \quad (2.14)$$

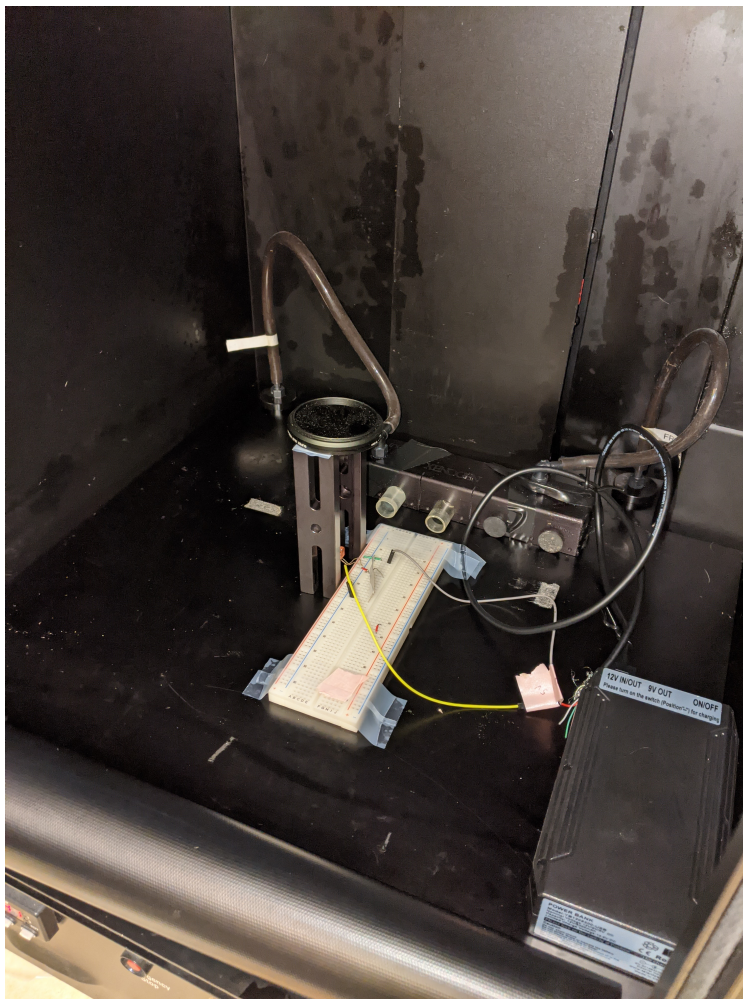


Figure 2.7: Imaging the LED within the IVIS using a neutral optical density filter.

$$\frac{\text{Total Subject Power}}{\text{Total LED Power}} = \frac{N \cdot 4\pi \cdot \text{Filter Attenuation}}{\text{LED Beam Solid Angle}} \cdot \frac{\text{Imaged Subject Counts}}{\text{Imaged LED Counts}} \quad (2.15)$$

$$\frac{\text{Total Subject Power}}{\text{Imaged Subject Counts}} = \frac{N \cdot 4\pi \cdot \text{Filter Attenuation}}{\text{LED Beam Solid Angle}} \cdot \frac{\text{Total LED Power}}{\text{Imaged LED Counts}} \quad (2.16)$$

Assumptions and Conversion Factor

One main assumption of this derivation is that both the subject and the LED act as point sources of light. This is more true for the LED than it is for the subject, as irregularities in material deposition within the test vials were observed to yield slightly differing measurements of the same subject, depending on the side viewed. In addition, it is assumed that the

LED emits uniformly within the solid angle of its beam. While this assumption cannot be construed to be particularly accurate on its own, it is mathematically equivalent to the more reasonable model assuming linearly degrading optical intensity from the center of the beam and delineating the beam solid angle according to the full-width half-maximum (FWHM). Ultimately, however, since the LED used was not finely characterized, further analysis on the dependence of its intensity on the emission angle was moot. For further calculations, the viewing angle of the LED was assumed to be 25° , as is common in production, with the half-angle, θ , assumed therefore to be 12.5° . Of note also is the fact that the angle at which the image is collected within the IVIS, the “IVIS Imaging Solid Angle”, drops out of the final formula due to the assumption that it is shared between each subject and the calibrating LED. In practice, effort was taken to ensure that this was the case by centering the subject vials within the camera field of view, as was done with the LED.

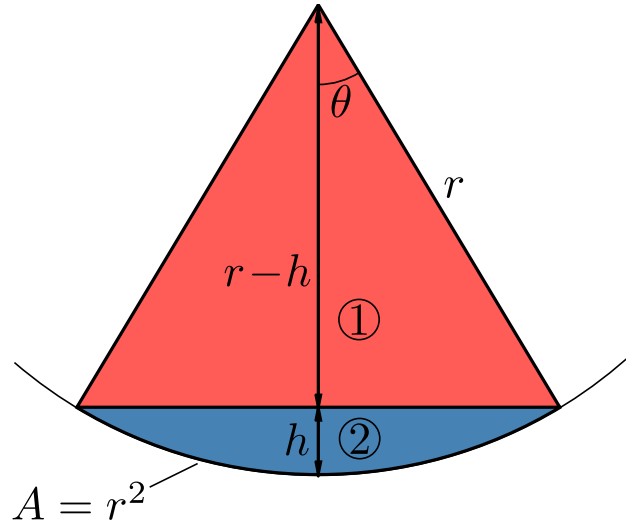


Figure 2.8: Geometric depiction of the incorporation of the LED viewing half-angle θ into the calculation of the solid angle subtended by its beam. The solid angle corresponds to the surface of the spherical cap marked in blue (region 2). [48]

Finally, the solid angle of the LED beam can be calculated using the viewing half-angle, $\theta = 12.5^\circ$, according to the following formula [48]:

$$\text{LED Beam Solid Angle} = 2\pi(1 - \cos \theta) = 0.1489 \text{ [steradians]} \quad (2.17)$$

Substituting this value, as well as a measured 23 nW for the “Total LED Power”, 1/45.43 for the filter attenuation, and 4426288 for the imaged LED counts over 0.5 seconds of exposure, we arrive at the desired conversion rule, shown below.

$$\frac{\text{Total Subject Power}}{\text{Imaged Subject Counts}} = 0.483 \text{ fW/count} \cdot \frac{10 \text{ sec.}}{\text{Subject Exposure Time}} \quad (2.18)$$

The parameter N has been decomposed into the form shown above due to the practical need to establish a convenient reference for the exposure time — 10 sec. was the value chosen because it allowed thorough and timely imaging of relatively dim samples, such as the QD-DOTA/Th-227 mixture mentioned in this chapter. For the brightest subjects, such as the LED during calibration, the exposure time was often scaled down to the minimum value of 0.5 sec. out of a need to avoid pixel saturation (which can lead to severe underestimation of subject light output). With this mapping established, quantitative evaluation of the results from the first experiment could proceed.

2.3 QD-DOTA Experiment Results and Conclusions

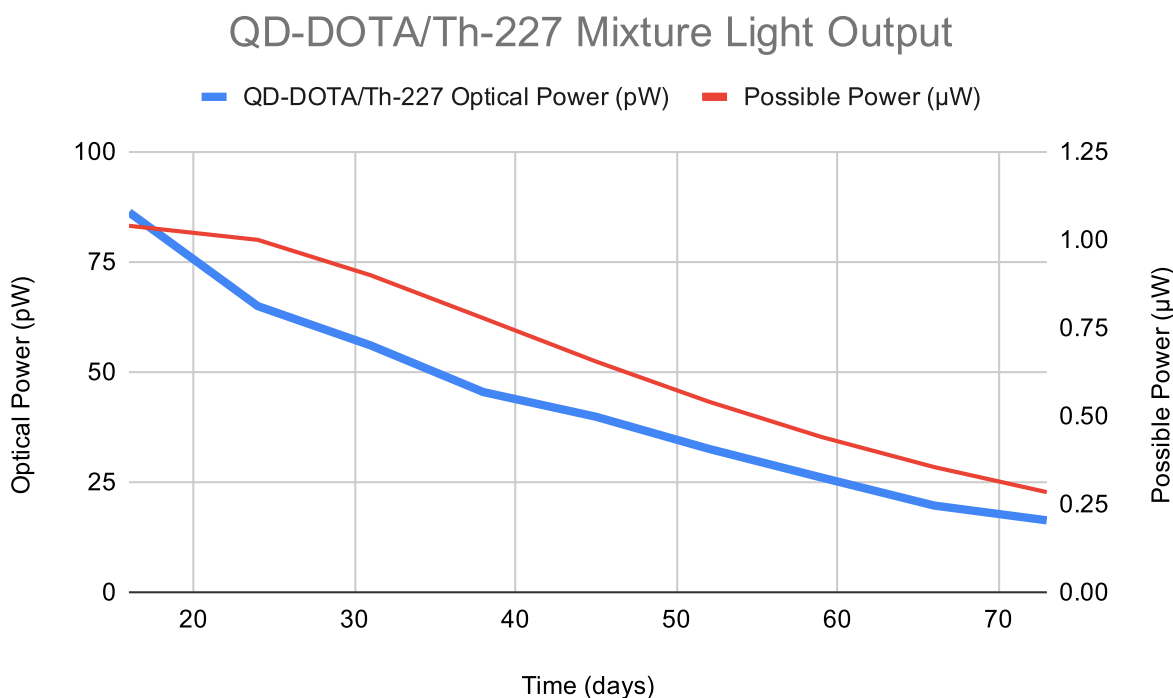


Figure 2.9: Comparison of light output from QD-DOTA/Th-227 mixture over time with the total power emitted through alpha radiation by a Th-227 sample with an initial activity of $11.6 \mu\text{Ci}$. Time is marked in terms of days after production of the Th-227.

While the results from this first experiment did indeed indicate that the application of the QD-DOTA solution to the radionuclide likely bolstered the light output of the radionuclide compared to the level attainable with just the radionuclide by itself in liquid solution (probably through Cherenkov radiation), the data showed that the conversion efficiency achieved

through this combination did not match the expectations of the initial hypothesis. Specifically, over the days the QD-DOTA/Th-227 mixture was imaged, the conversion efficiency, calculated as the measured optical power (according to the formula from the previous section) divided by the possible emitted power (as visualized in Figure 2.3 for a sample with higher activity) hovered around 0.006%, indicating that the conjugation had either not actualized or was otherwise immaterial to the energy conversion process. However, this same efficiency characterization reveals that the decay in the light output from the QD-DOTA/Th-227 vial generally tracks the shape of the curve for the possible emitted power when only alpha radiation is considered, as can be seen in Figure 2.9. This affirms that the light generated comes mainly through the scintillation of the quantum dots in response to the alpha radiation, rather than through some other process. Given the highly approximate nature of the measured activity values for these vials in the first place, this last point represents the most essential conclusion that can be drawn from this analysis.

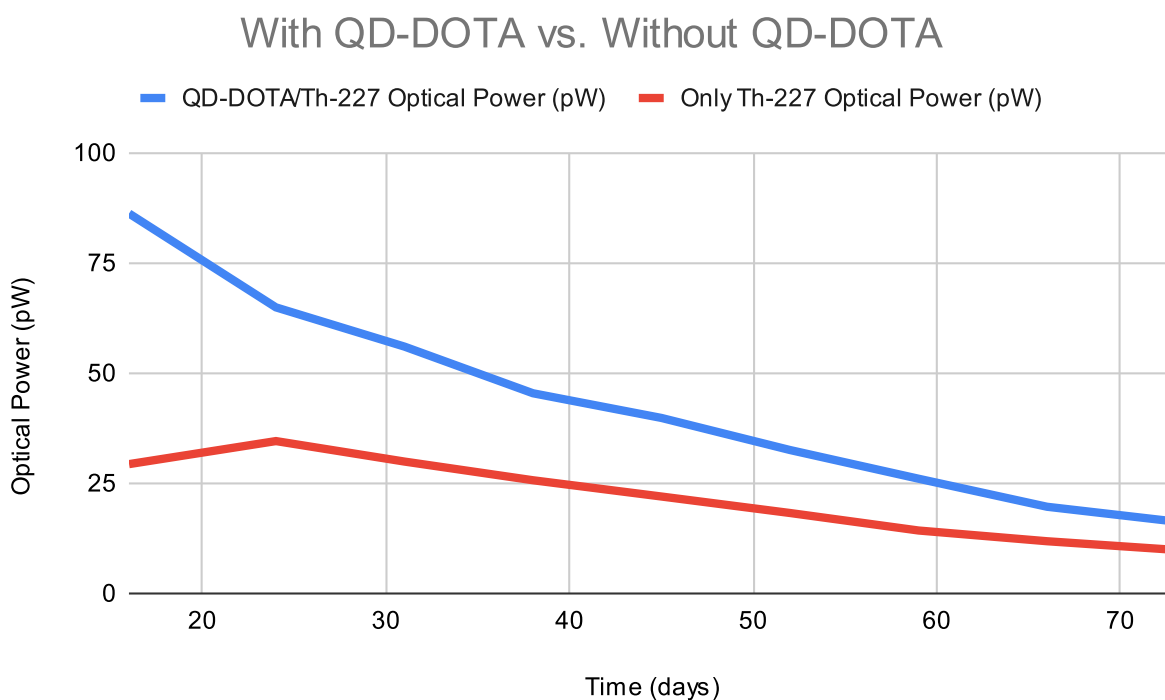


Figure 2.10: Comparison of the light output from the QD-DOTA/Th-227 mixture (initial activity around $11.6 \mu\text{Ci}$) with light output from the vial containing only Th-227 in solution (initial activity around $6.2 \mu\text{Ci}$). Time is marked in terms of days after production of the Th-227.

QD-DOTA Efficacy

Be that as it may, the benefit in terms of light output from this scintillation seems to be marginal. Illustrative is the comparison between the light output from the QD-DOTA/Th-227 vial and the vial containing only Th-227 in solution, depicted in Figure 2.10. Certainly, the former seems to emit more light than the latter, but, if a scaling were to be done to put these two sets of data on level footing with regard to initial activity, the difference would reduce significantly. Due to the approximate nature of the initial activity values (as addressed in Section 2.1), this scaling has not been applied in the presented data. Suffice it to say, however, that the combination of QD-DOTA and Th-227 did not yield optimal performance with regard to light generation.

A quick calculation could impart insight on whether the DOTA conjugation strategy could have meaningfully improved the energy conversion efficiency to begin with.

$$A_{tot}(t = 0) = \lambda_{Th} N_{Th}(t = 0) \Rightarrow N_{Th}(t = 0) = A_{tot}(t = 0) / \lambda_{Th} \quad (2.19)$$

This yields that there were 3.234×10^{12} Th-227 atoms initially present in the QD-DOTA/Th-227 mixture. In addition, there were 160 pmol of QDs in this mixture, implying that 9.635×10^{13} QDs were present. There were therefore initially (and thereafter) around 30 quantum dots for each radionuclide. This means that the conceptual model illustrated in Figure 2.1, in which multiple radionuclides are attached to a single quantum dot, is in fact not applicable to this scenario at all. In general, this model would require the number of radionuclides to far outstrip the number of quantum dots, necessitating that each quantum dot converts alpha radiation coming from many directions at any given time. In addition, alpha particles emitted outward from the quantum dot must travel through the solvent medium, depositing energy all the while, before possibly hitting another quantum dot in the solution. In conclusion, whether or not the conjugation occurred successfully, it was unlikely to change the outcome in terms of the amount of light generated by the mixture.

A More Accurate Model

A simple model, in which the scintillator or phosphor material is packed around the radionuclides, is more applicable to this scenario, and aligns conceptually with studies conducted in the literature on “indirect” conversion for alphavoltaics involving a thin phosphor/scintillator layer used to augment system energy conversion efficiency [4, 23, 52, 59]. The limiting case for this model, in which maximal packing has occurred, seems more efficient in general, as it allows for the emitted alpha particles to deposit as much of their energy as possible within the light-generating material, rather than the solvent medium. However, the presence of an aqueous solvent (PBS) can only interrupt this sort of packing — removing it could improve the energy conversion efficiency by closing the distance between the light-generating particles and the radionuclides, as well as by virtue of the fact that alpha particles deposit less energy in air than in aqueous media [33].

Evaporation

This was tested empirically by safely evaporating the QD-DOTA/Th-227 solution within an iodine fume hood on the 93rd day following production of the Th-227. The mixture was imaged before and after the evaporation, with precipitate clumps of QDs forming conspicuously within the centrifuge tube after the evaporation. In addition, the mixture was rehydrated and imaged in steps using deionized water (DI H₂O), with the final volume brought to 200 μ L. The results of this experiment are shown in Figure 2.11.

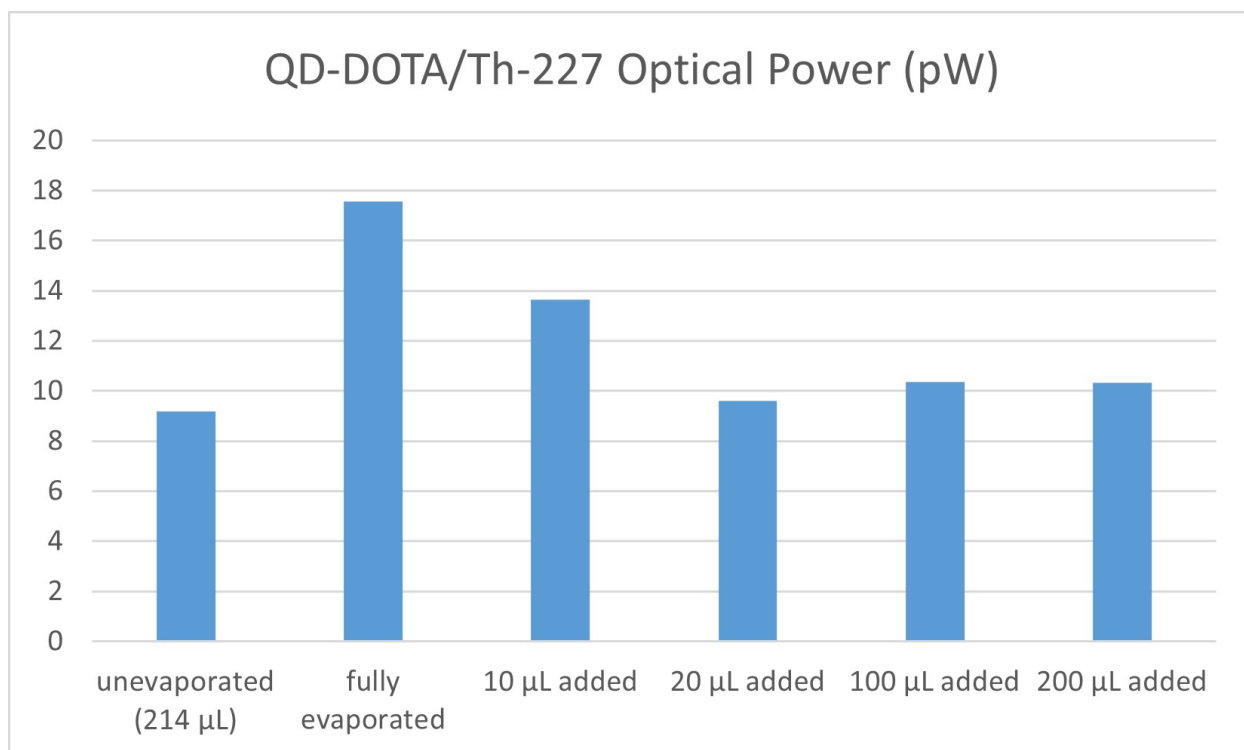


Figure 2.11: Changes in light output of QD-DOTA/Th-227 mixture due to evaporation of the aqueous solvent and subsequent rehydration of the resulting precipitate clumps with deionized water. After 20 μ L of water was added, the precipitate clumps dissolved back into solution.

As hypothesized above, the removal of the aqueous solvent did seem to directly improve the light output of the mixture. A challenge of this procedure was that it was difficult to determine exactly whether the distribution of the radionuclides within the mixture remained uniform, as is generally a fair approximation within liquid solution, following evaporation. However, even if all the gains in light output arose because the liquid solvent was no longer present to effectively shield the alpha radiation, this small experiment shows that evaporation can have a noticeably positive effect on the overall energy conversion efficiency. A

significant additional benefit of this evaporation procedure is that the mixture no longer occupies as much volume. As a result, a system of sequentially mixing and then evaporating the scintillating/phosphorescent material and radionuclide is proposed to ensure system compactness, as will be elaborated in the next chapter.

To demonstrate system viability following this experiment, alternatives to the quantum dot scintillator needed to be explored. Based on these results, it was inferred that a scintillator/phosphor with relatively large particle size and high quantum yield would likely produce better results, by collecting more alpha radiation energy and converting as much of it to light as possible. To this end, a host of phosphorescent materials were considered and evaluated in a similar experimental setup, with the results presented and discussed next.

Chapter 3

Conditions for Optimal Light Generation

3.1 Finding the Best Phosphor

Table 3.1: Different scintillating/phosphorescent materials used in second experiment. D50 signifies that the indicated size approximately reflects the median value.

Material Name	Identifier	Supplier	Quantum Yield	Particle Size	Emission Wavelength
Solid Form CdSSe-ZnS Core/Shell QDs [37]	QSP-645	Ocean NanoTech	>50%	-	645 nm
$\text{NaY}_{0.77}\text{Yb}_{0.20}\text{Er}_{0.03}\text{F}_4$ [2, 47]	SA-UCPh	Sigma-Aldrich	~3%	1 to 5 μm (D50)	940 to 980 nm
$\text{Y}_{1.92}\text{Eu}_{0.08}\text{O}_3$ (YEO) [51, 62]	SA-YO	Sigma-Aldrich	~100%	4 to 8 μm	611 nm
YYG 560 200 Isiphor® [64]	YYG 560	Sigma-Aldrich	>90%	19.5 to 21.5 μm (D50)	560 nm
SGA 555 100 Isiphor® [45]	SGA 555	Sigma-Aldrich	>90%	12 to 14 μm (D50)	555 nm
Rare Earth Doped Phosphor Nanoparticles [40]	SA-620	Sigma-Aldrich	-	10 nm	620 nm

Motivation and Experimental Design

As was clear from the results of the first experiment, an alternative material for generating light was necessary for this strategy of alpha power source miniaturization to succeed. In addition, it was worthwhile to identify whether the poor overall energy conversion efficiency seen in the first experiment would be replicated without the DOTA conjugation. To identify the best material and conditions for generating light from a Th-227 alpha source, samples of many different commercially-available scintillators and phosphors were procured, as listed in Table 3.1. For experimentation purposes, each of these materials was confirmed to not phosphoresce at a significant level in response to ambient lighting. Th-227 in nitrate form

was then acquired from ORNL, with 3 mCi dissolved in 200 μL of HCl solution. Glass scintillation vials were then prepared containing 2 mg (or the equivalent) of each of the listed materials and 5 μL of this Th-227 solution, yielding an approximate initial activity of 75 μCi for each vial. In each case, the phosphor/scintillator was deposited and measured within the vial before the radionuclide was inserted via pipette. The exact amount of the Th-227 solution used for each vial in this comparison was likely slightly in excess of 5 μCi , due to the uncalibrated nature of the pipettors used to do the transfer.

For each material, an additional identical vial was prepared and then evaporated, leaving two vials for each material containing the same amount of the radionuclide over the course of the experiment: one unevaporated and one evaporated. Finally, one control vial of 5 μL of the original Th-227 solution (labeled “CONTROL” in plots) was prepared slightly belatedly and left unevaporated. For thoroughness, an identical evaporated control vial should have been prepared as well, however, insufficient Th-227 solution remained for this to be done. Future experiments will include this consideration, as it will reveal definitively whether the “background” light emitted without the presence of a phosphor indeed arises due to Cherenkov radiation or not, as, in the absence of a solvent medium with a refractive index noticeably higher than 1, like water, this radiation should be significantly reduced [39].

Initial Results

The results of this investigation are shown in Figures 3.1, 3.2, and 3.3. As is apparent from these plots, regardless of whether evaporation has occurred or not, vials containing SA-YO seem to produce the most light by far. This is not particularly surprising considering that this material, yttrium oxide doped with europium, has a reported quantum yield/efficiency (metrics describing the intrinsic efficiency with which a material converts incident radiation into light) of close to 100% [51]. When evaporated, the vial containing SA-YO achieves around 2% average energy conversion efficiency, which indicates that efficiency performance similar to that achieved in RTGs can be derived in a much smaller form factor using this light generation and harvesting method [56]. This is the case even after accounting for the $\sim 20\%$ harvesting efficiency of silicon photovoltaics and 50% conversion efficiency of a low-power harvesting circuit, which would yield $\sim 0.2\%$ total conversion efficiency — indeed, implanted nuclear batteries had efficiencies only slightly higher than this [56].

Also of note is the fact that the growth and decay of the light output of each vial generally seems to track the “possible power” curve fairly well. This is most apparent in the plots with a logarithmic scale applied to the vertical axis. Naturally, due to inconsistencies in the exact side of the vial imaged within the IVIS and the nonuniform distribution of the phosphor and radionuclide within each vial, these sometimes large variations are expected. However, the general trend is fairly clear, and this further confirms the assertion from the previous chapter that the suggested alpha particle emission dynamics are responsible for light generation in this context. The minimum amount of light generated can be seen to correspond to the control vial, as expected. The unevaporated vial containing SA-620, which had the lowest

light emission among the vials shown here, seemed to track the light output of this control vial but did not descend noticeably below it.

Interestingly, the effects of evaporation seem more unclear. For the materials emitting the most light, evaporation results in greater light production compared to the unevaporated case. However, for QSP-645 and SA-UCPh, evaporation results in seemingly less light output. In the case of QSP-645, which is the same quantum dot material used in the previous experiment in solid form (not in a dispersion), it is possible that the distribution of discrete QD clumps did not align well with the radionuclide in the evaporated vial, precluding efficient light generation. For SA-UCPh, further investigation is required, although phosphor distribution issues are once again a likely culprit. However, this phosphor could not be characterized well by this experimental setup to begin with, as its emission spectrum lies far outside of the efficient conversion range of the IVIS CCD camera [19]. In general, provided that the phosphor and radionuclide are not moved farther apart as a result, evaporation seems to be beneficial from a light generation perspective. Certainly, the prospect of adding more radionuclide in the volume vacated by the solvent is an extremely attractive one, as it would allow for potentially much greater light output (theoretically tracking linearly with the amount of radionuclide).

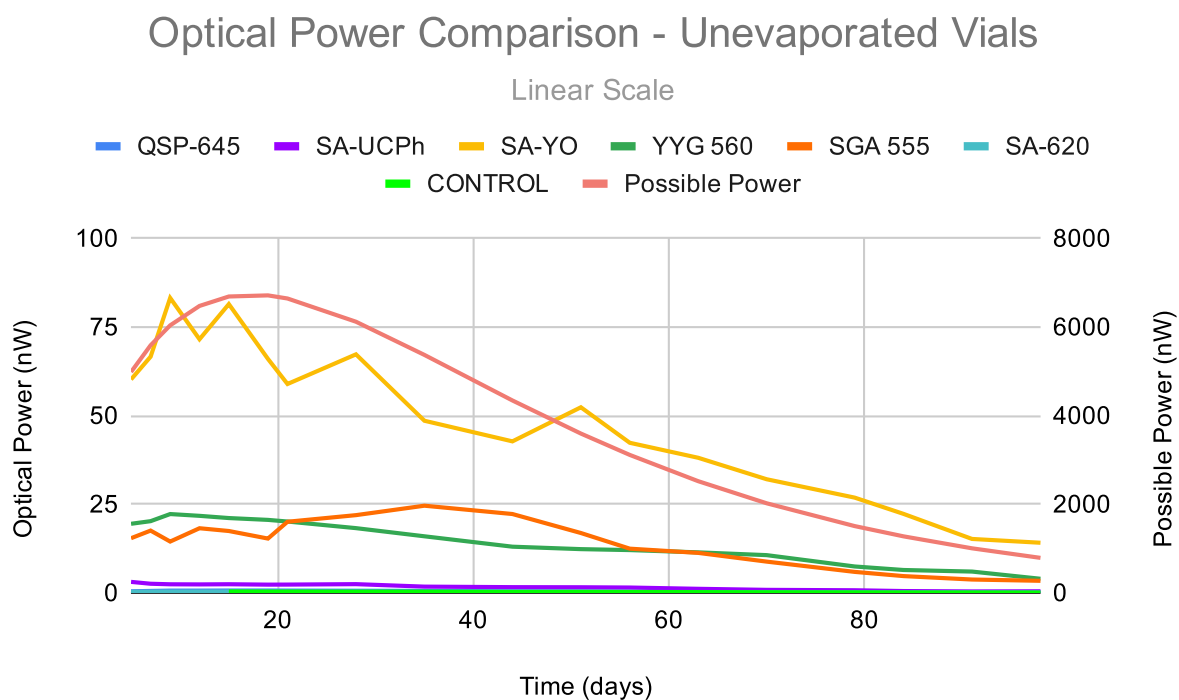
Overall, the “best” phosphor as determined by this analysis was SA-YO. In addition to producing the most light in all situations, this phosphor emits red light, which is compatible with efficient harvesting through silicon photovoltaic structures (although, perhaps, infrared radiation is generally more compatible). Samples of SA-YO were prepared varying the amount of the phosphor, as well as the amount of the radionuclide, in order to quantify the effects of changing these parameters on the system energy conversion efficiency and absolute light output. These results are presented in the next section.

3.2 Optimally Combining the Radionuclide and Phosphor

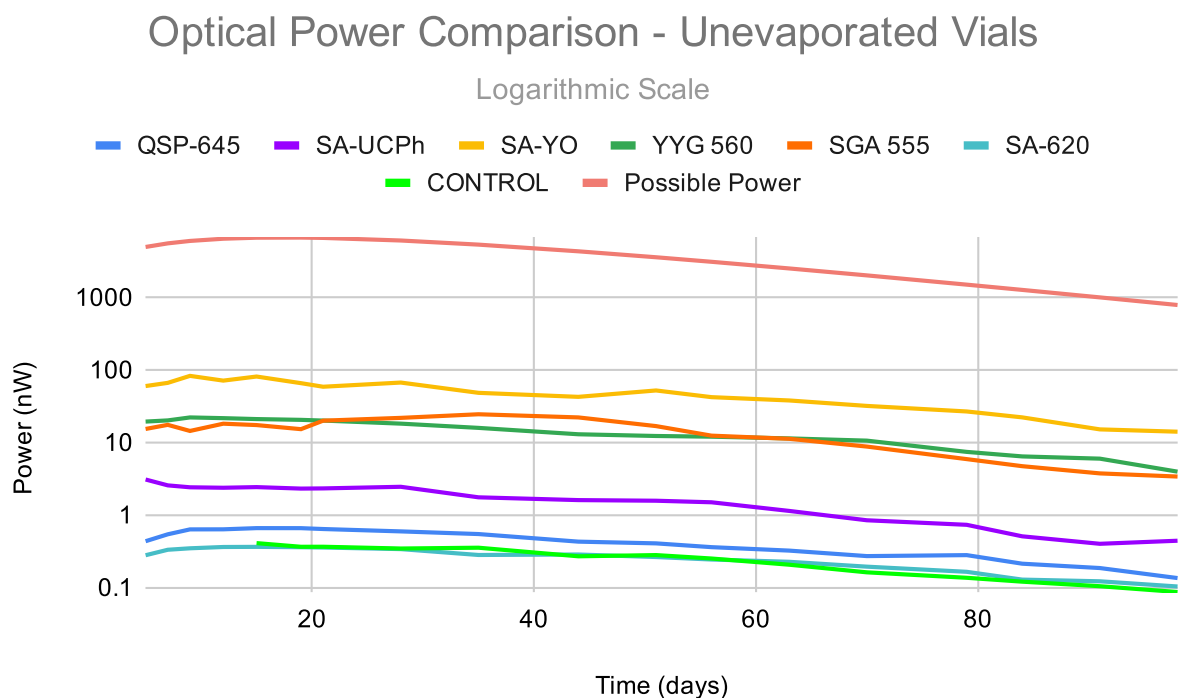
Samples of varying amounts of SA-YO phosphor were prepared on the 12th day following production of the Th-227. Th-227 solution was added to these vials to produce sweeps of the phosphor amount (with the amount of Th-227 constant at 5 μL , approximately equivalent to 75 μCi) and Th-227 amount (with the amount of the phosphor constant at 16 mg). Based on the results presented in the previous section, evaporation was presumed to lead to higher light output in general. As a result, most of the vials prepared for these sweeps were evaporated on the 19th day following production of the Th-227.

Comparison Before Evaporation

To establish a baseline, the light output from these vials was compared immediately before evaporation, with Figure 3.4 depicting the results. As can be seen in Figure 3.4(a), increasing the amount of the phosphor while keeping the amount of Th-227 constant leads generally to

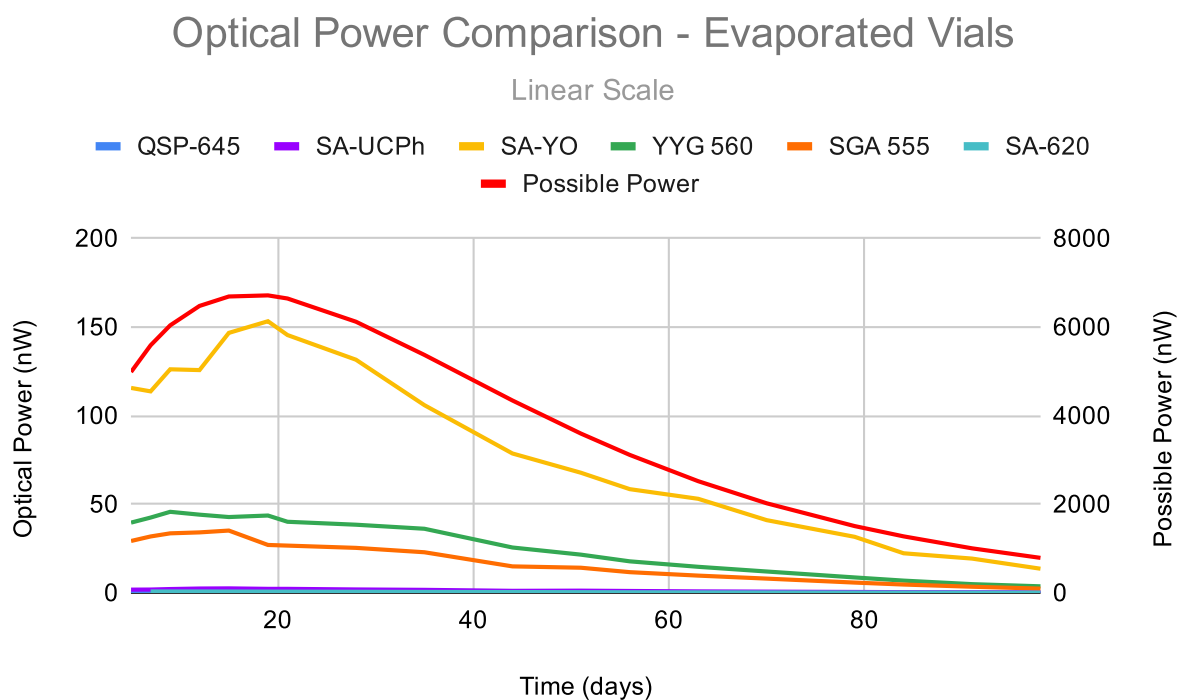


(a) Linear scale applied to the vertical axes; only possible power scaled according to the right axis.

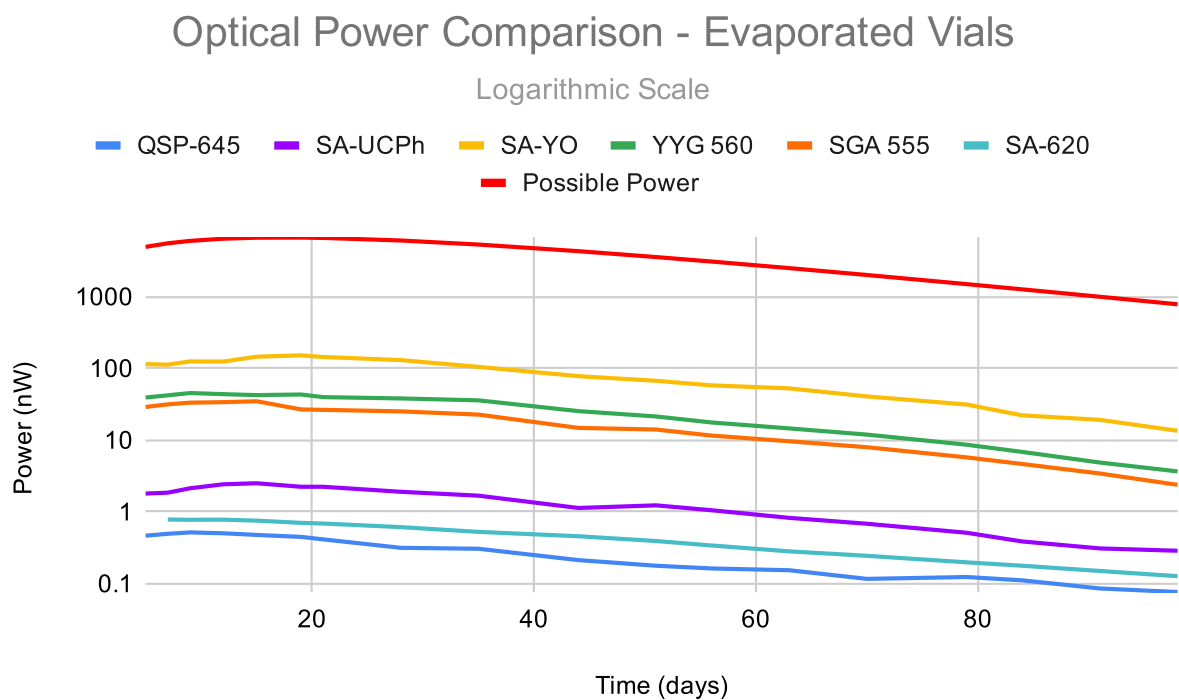


(b) Logarithmic scale applied to the vertical axis.

Figure 3.1: Light from unevaporated vials with 2 mg of phosphor and 5 μL of Th-227 solution compared against the total power emitted by the same amount of Th-227.

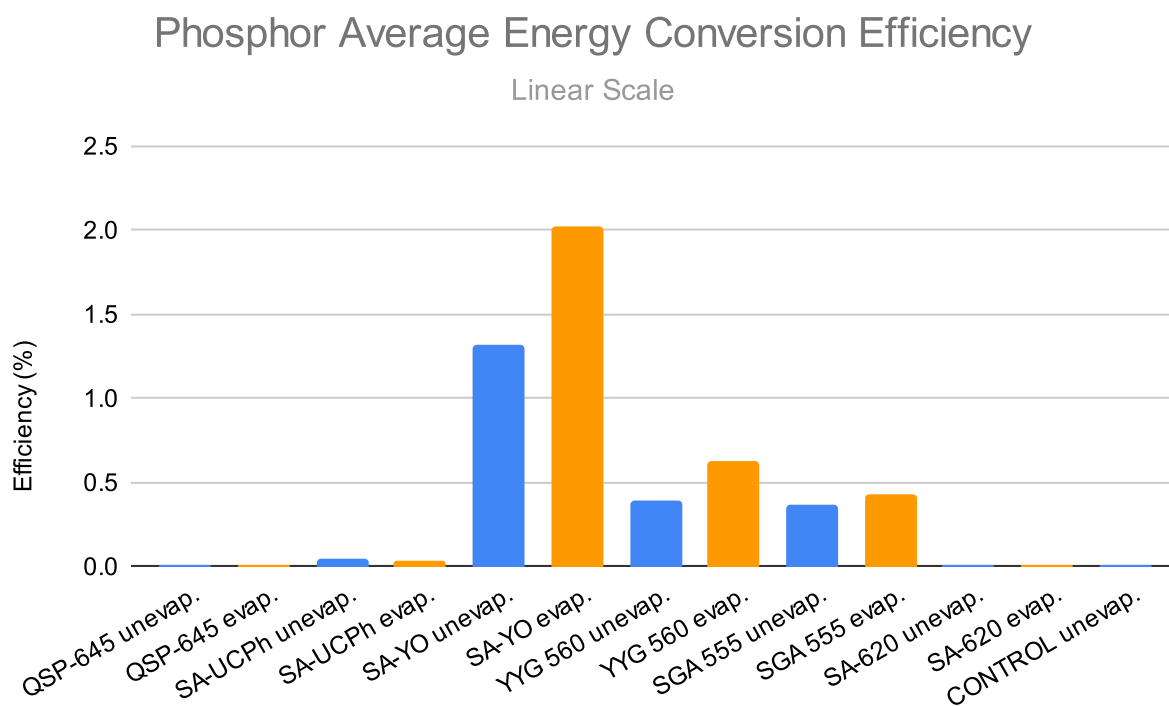


(a) Linear scale applied to the vertical axes; only possible power scaled according to the right axis.

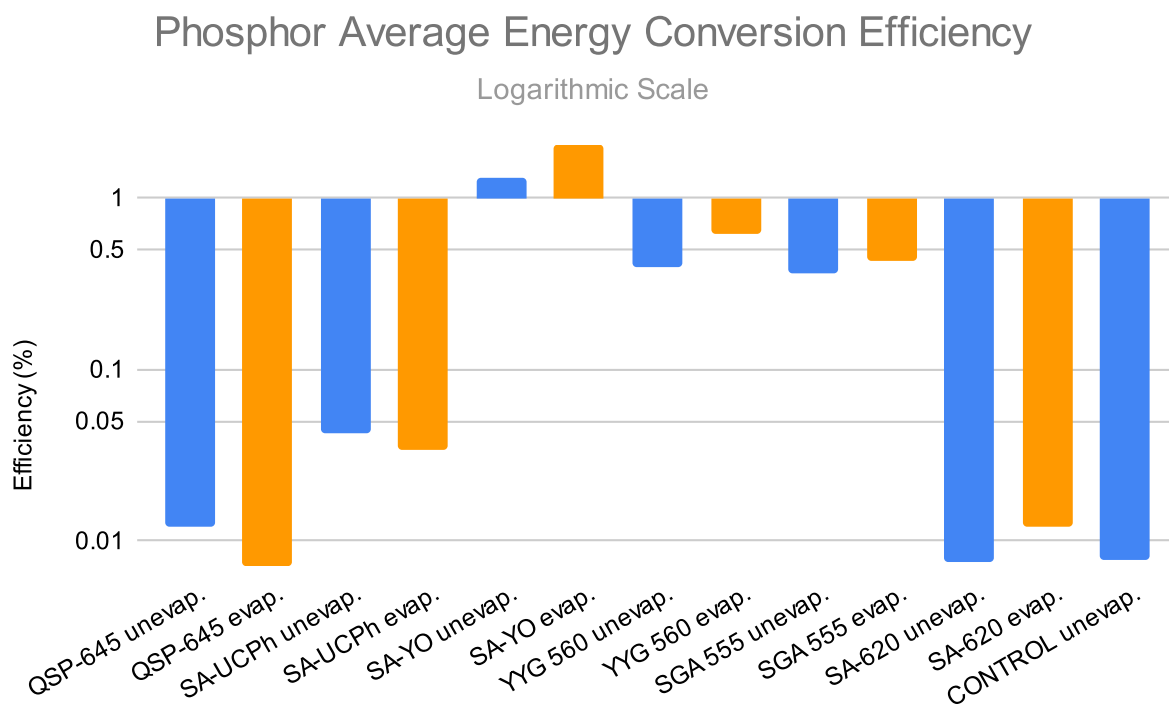


(b) Logarithmic scale applied to the vertical axis.

Figure 3.2: Light from evaporated vials with 2 mg of phosphor and, initially, 5 μL of Th-227 solution compared against the total power emitted by the same amount of Th-227.

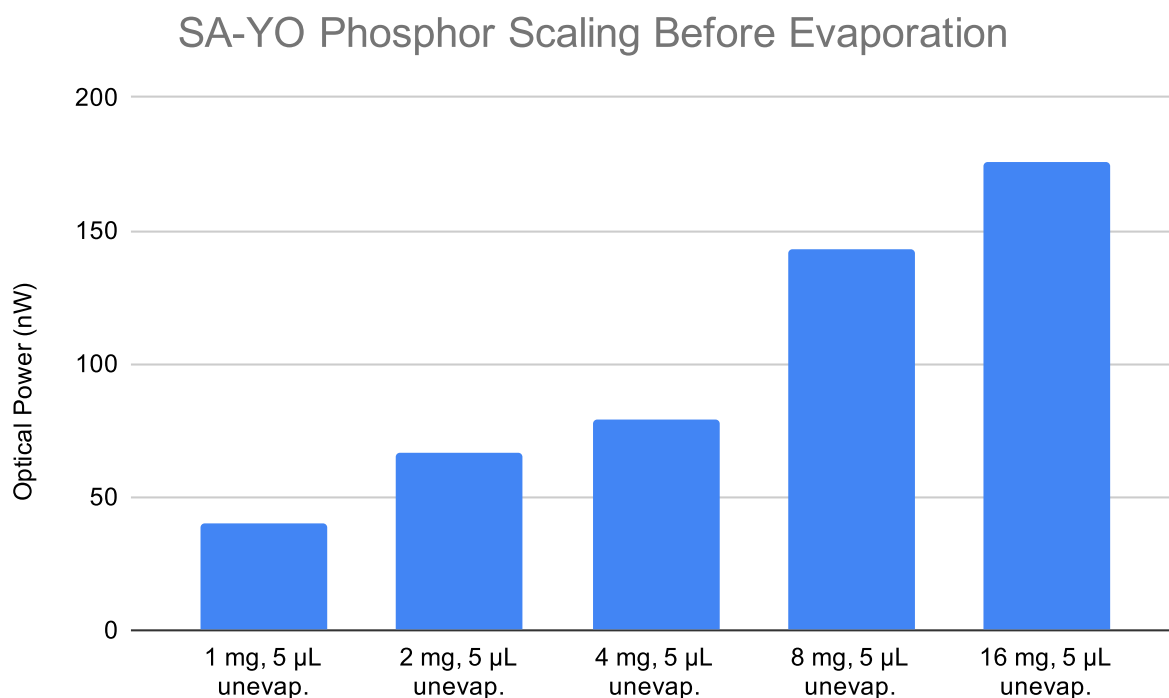


(a) Linear scale applied to the vertical axis.

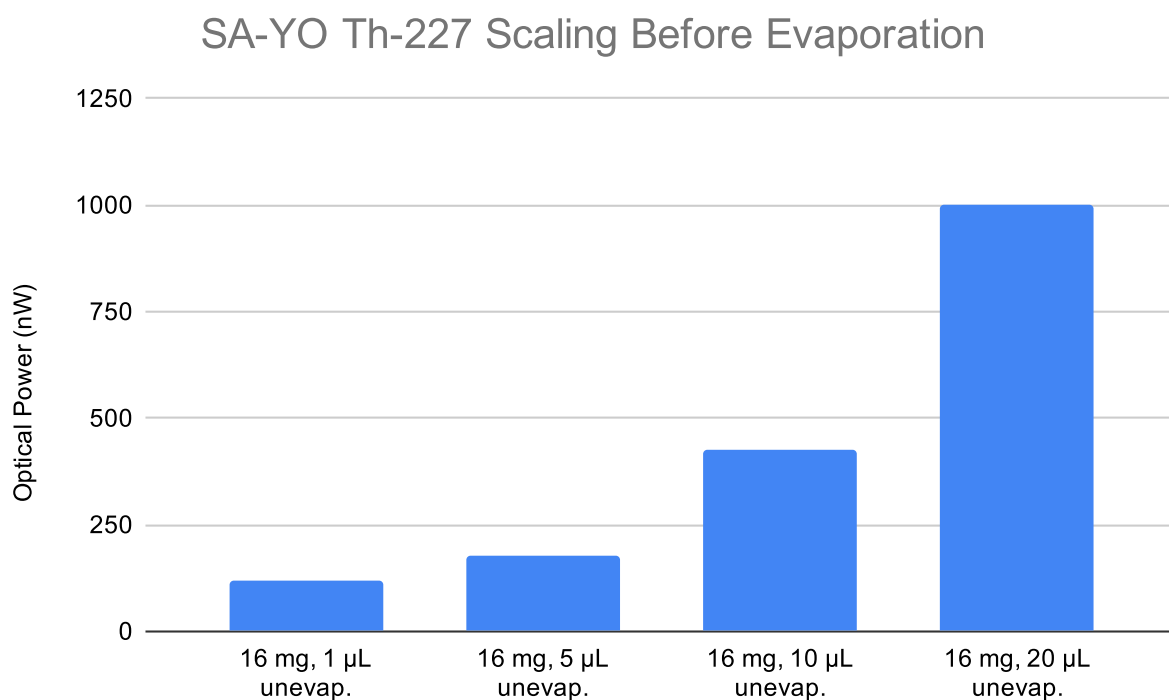


(b) Logarithmic scale applied to the vertical axis.

Figure 3.3: Comparison of the average energy conversion efficiency for different vials containing 2 mg of phosphor initially with 5 μ L of Th-227 solution.

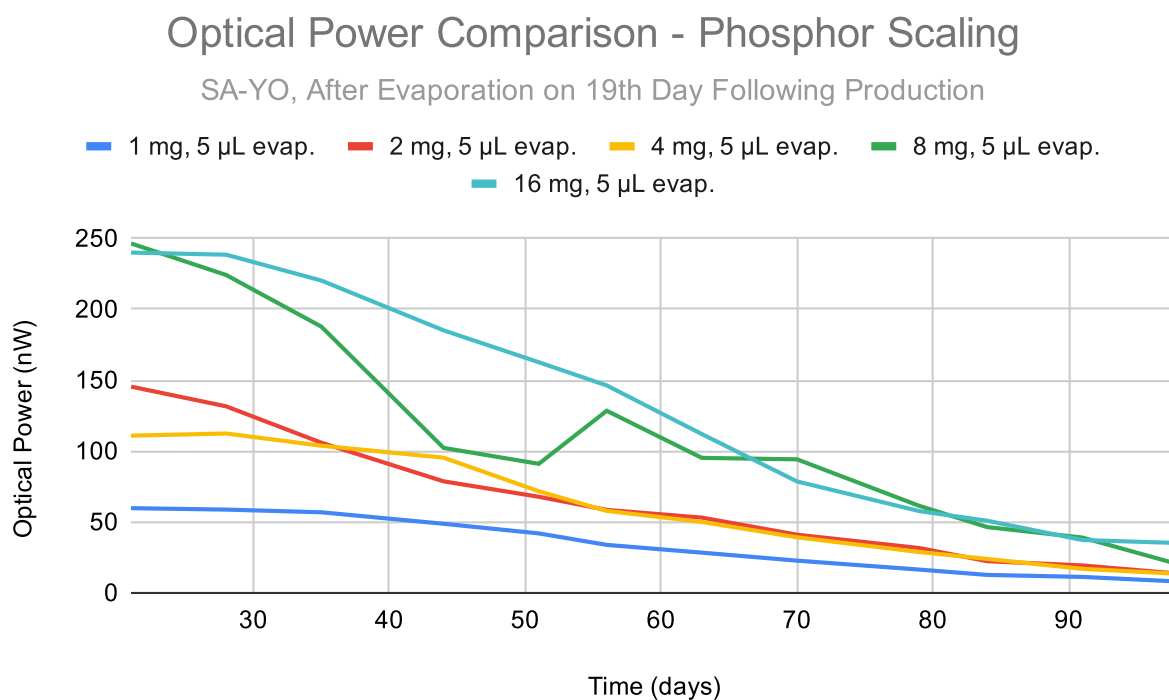


(a) Phosphor scaling before evaporation, with Th-227 amount constant at 5 μ L.

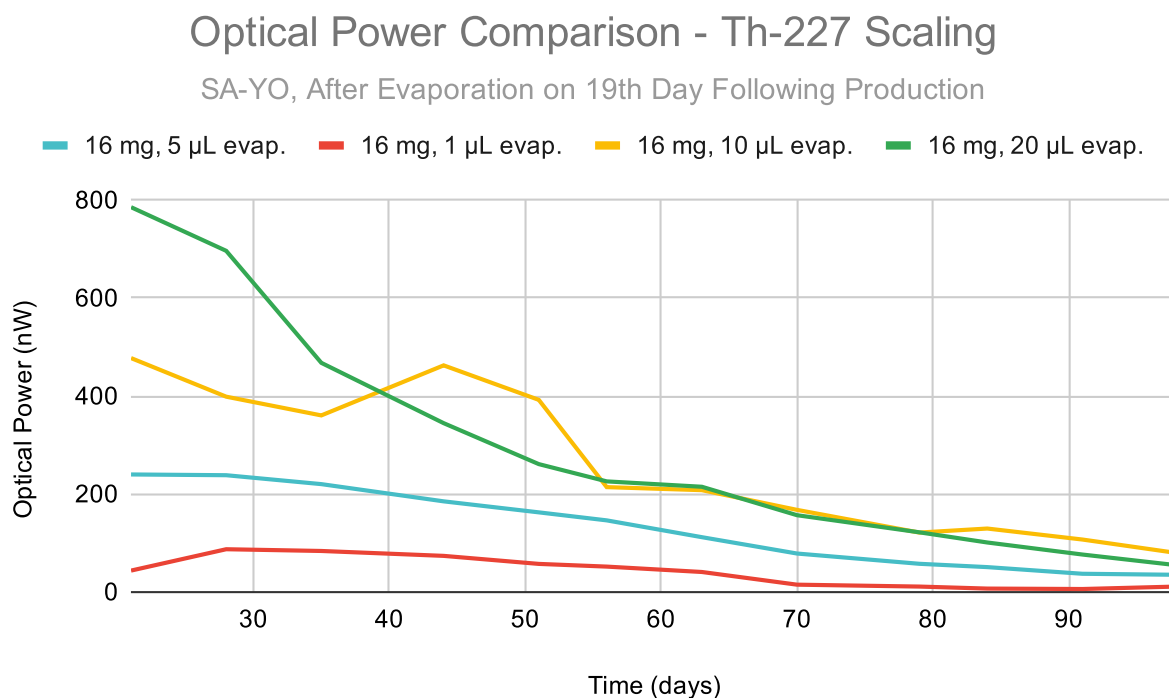


(b) Th-227 scaling before evaporation, with phosphor amount constant at 16 mg.

Figure 3.4: Comparison of light output before eventual evaporation of vials containing SA-YO when the phosphor and radionuclide amount are scaled.

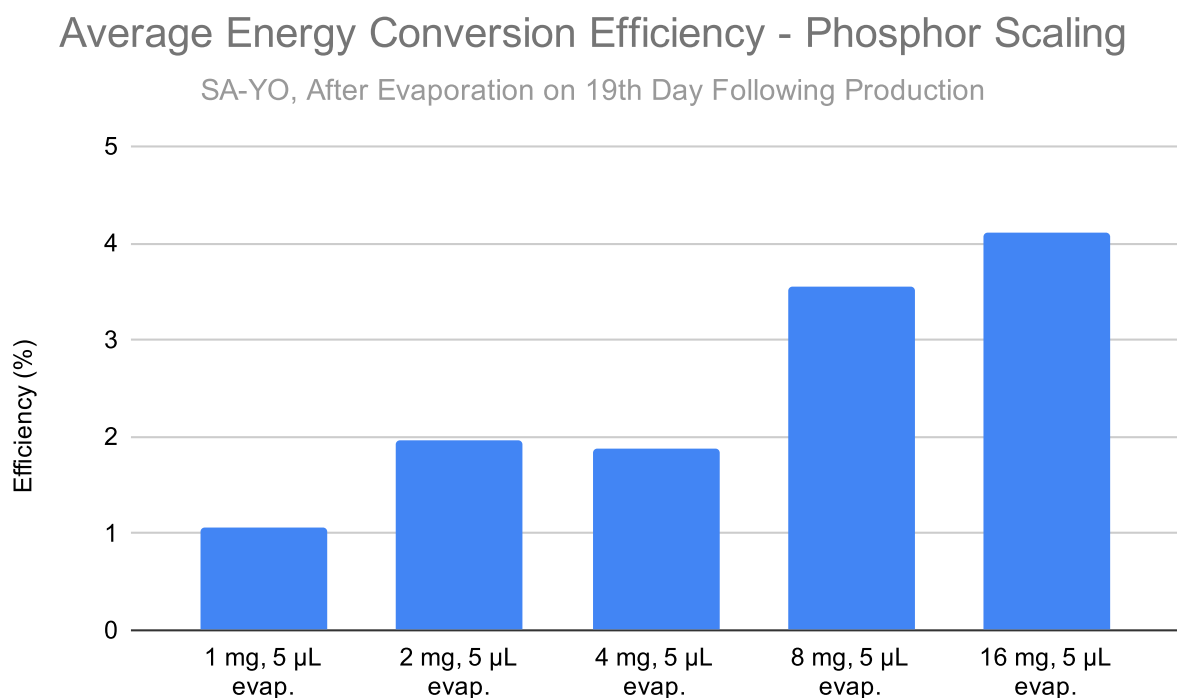


(a) Phosphor scaling after evaporation, with Th-227 amount constant at 5 μL .

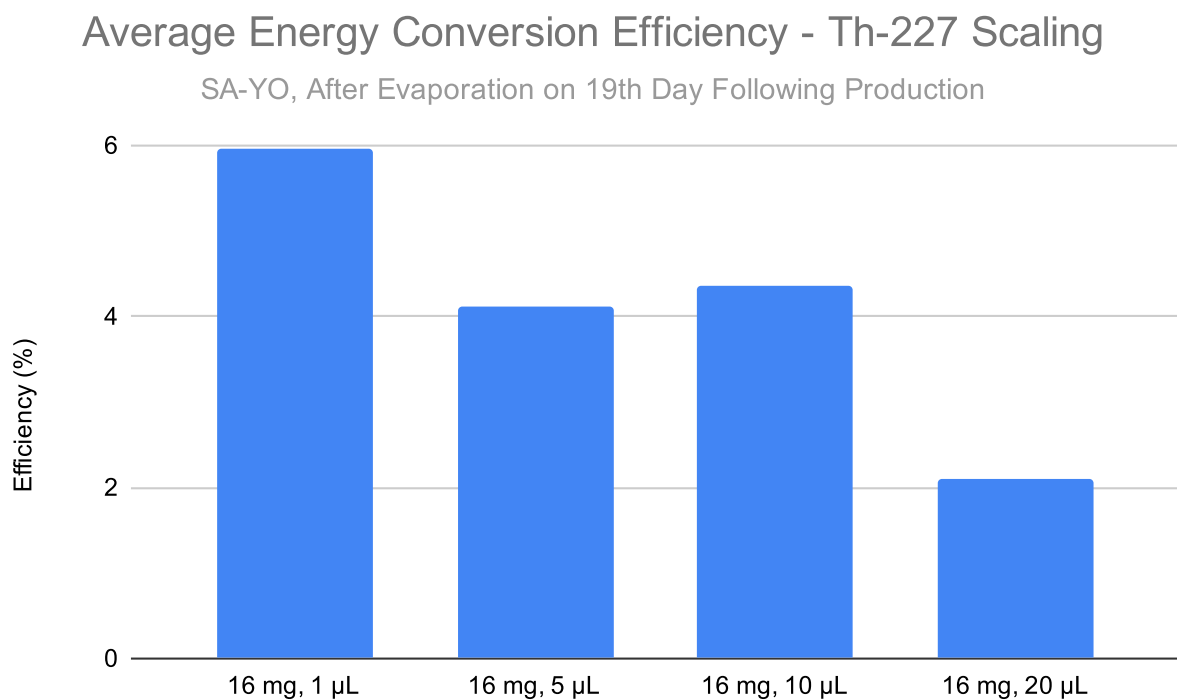


(b) Th-227 scaling after evaporation, with phosphor amount constant at 16 mg.

Figure 3.5: Comparison over time of light output after evaporation of vials containing SA-YO when the phosphor and radionuclide amount are scaled.



(a) Phosphor scaling average efficiency after evaporation, with Th-227 amount constant at 5 μ L.



(b) Th-227 scaling average efficiency after evaporation, with phosphor amount constant at 16 mg.

Figure 3.6: Comparison over time of average energy conversion efficiency after evaporation of vials containing SA-YO when the phosphor and radionuclide amount are scaled.

higher light output, although the exact relationship is unclear. The relationship is uncertain because the distribution of the phosphor and Th-227 within any single vial was almost certainly very different from that of any other vial, due to the flat bottom (slightly less than 1.5 cm in diameter) and relatively large volume of the scintillation vials used. This issue can be mitigated in future experiments by using a vial with a conical end, so as to more completely collect the phosphor and radionuclide. In addition, the presence of lumps of phosphor caked along the sides of the vial directly impacted imaging efforts by imparting large angular variation (up to 40% for the most irregular distributions) on the amount of light escaping the vial. This was especially apparent in the vials containing 16 mg of the phosphor, as the excess phosphor seemed to contribute more toward impeding the light produced at the phosphor-radionuclide interface (further within the vial) than producing light itself.

Inspecting Figure 3.4(b), increasing the amount of Th-227 while keeping the amount of phosphor constant seems to result in clearly greater light output as well, with a generally linear trend seemingly broken by the vial containing 16 mg of SA-YO phosphor and 1 μL of the Th-227 solution. Oddly enough, the light output of this vial seemed to increase significantly between the day it was prepared and the day it was evaporated. This did not match the progression of the light output from any of the other vials, which seemed to track the expected multi-exponential behavior overall. This sort of behavior could be explained by the presence of mechanical formations within the mixture, perhaps such as bubbles, that become more compact over the course of many days, thereby increasing the proximity of the radionuclide and phosphor and improving the energy conversion efficiency. Incidentally, a vial containing the same amount of phosphor and radionuclide was prepared and left unevaporated for an additional point of comparison. On the same day that the vial in question was evaporated, this additional vial produced about four times less light. The higher value is presented in Figure 3.4(b) to indicate that the observed value is indeed possible; however, the lower additional value would fit a linear trend much better, as would otherwise be expected with a linearly increasing amount of radionuclide. At the very least, the anomalies discussed here indicate that the specific process used to mix the phosphor and radionuclide plays a significant role in determining the eventual light output and energy conversion efficiency of the system.

One important practical note for the measurements of the vial containing 16 mg of SA-YO and 20 μL of the Th-227 solution (before evaporation) is that the light produced by this vial would invariably saturate the IVIS camera until the 35th day following production of the Th-227 (16 days after evaporation). As a result, the same neutral density filter used for the initial IVIS LED calibration was used to image this vial, except at a more transparent blocking setting. Filter transmission at this setting was confirmed empirically to be about 1/7.4, and this factor was used to scale up counts imaged through the filter.

Comparison After Evaporation

Evaporation results in increased light output for all vials in the phosphor scaling sweep, with the average ratio of the final and initial values around 1.5 (where “final” refers to the

first measurement of the evaporated vials conducted two days after evaporation). However, some vials see greater increases in light output than others, perhaps due to initially favorable physical arrangements of the radionuclide and phosphor. In particular, the vial containing 2 mg of SA-YO sees its light output at least double following evaporation, maintaining similar performance to the vial containing 4 mg of SA-YO. This suggests that the effective interface between the phosphor and radionuclide within each of these vials is similar, despite the fact that one of them has two times the amount of phosphor.

In contrast, evaporation seems to do less and less to increase the light output as the amount of Th-227 increases. The exact explanation for this phenomenon is unclear, and this issue will be investigated further in future experiments. To eliminate one possible explanation, the evaporation process was confirmed to not affect the relative activities of the vials in this sweep, as is shown by the uncalibrated activity measurements presented in Table 3.2, which display the expected linear scaling of the activity. Despite this uncertainty regarding the effect of evaporation on light generation with higher amounts of radionuclide, the main benefit of evaporation remains the greatly minimized total volume of the mixture, which contributes directly to device miniaturization, as discussed previously.

Table 3.2: Relative activities (in terms of arbitrary units) of the vials used in the SA-YO phosphor amount sweep. The unevaporated vial (16 mg, 1 μL unevap.) was prepared in addition to (i.e., separately from) the evaporated vial with the same amount of radionuclide and phosphor.

SA-YO Vial	Activity (a.u.)
16 mg, 1 μL unevap.	3 to 4
16 mg, 1 μL evap.	4
16 mg, 5 μL evap.	18
16 mg, 10 μL evap.	36
16 mg, 20 μL evap.	70

Phosphor Scaling Conclusions

Comparing the time evolution of the light output from the vials in the phosphor scaling sweep, diminishing returns seem to arise at about 8 mg of the SA-YO phosphor, with the light generated by the 16 mg vial representing only a marginal increase on average. This implies that the light-producing interface is more or less established within the vials used once 8 mg of the phosphor has been inserted. This is more likely to reflect on the coverage of the phosphor across the bottom of the vial, where the radionuclide is deposited, than the intrinsic mixing properties of the radionuclide and the phosphor. As a result, it is highly possible that, within a container that collects the radionuclide and phosphor together, such

as a vial with a conical end, maximum light output could be achieved using a smaller amount of phosphor, for the same amount of radionuclide. Another aspect of this experiment that impacts these results is the fact that the radionuclide and phosphor were not actively mixed together once both were inserted within a vial. It is therefore possible that the maximum light output for any given combination of radionuclide and phosphor could be augmented through the simple act of mixing the two thoroughly, although this is made difficult practically due to the contamination of the mixing device and resulting need to dispose of it safely.

Radionuclide Scaling Conclusions

Examining Figure 3.5(b), as well as Figure 3.4(b), it is clear that, in general, increasing the amount of radionuclide while keeping the amount of phosphor the same can lead to (potentially significantly) greater light output, especially soon after the radionuclide and phosphor are combined. However, the later data points from Figure 3.5(b) imply that the light output from the vial containing 16 mg of the SA-YO phosphor (as is the case for all vials in this sweep) and 20 μL of the original Th-227 solution falls to a similar level as that of the vial containing half the amount of the radionuclide. Assuming that this occurs universally, this would suggest that the light generating capability of the phosphor is being degraded by damage imparted by the radiation, which is a known phenomenon examined in the literature for other phosphors [52]. Naturally, the amount of this damage would scale with the system radioactivity. This would mean that while the initial instantaneous power might scale with the amount of the radionuclide, the effective lifetime of the power source would not exceed some limit. However, further investigation with higher activity values is required to ascertain that this light output drop-off is indeed caused by radiation damage and not some other experimental issue.

Broader Outlook and Practical Implementation

In many ways, this experiment raised more questions than it answered. In particular, future experiments will need to confirm the exact effects of evaporation on light output, the limit on light output gains with phosphor scaling in more closely packed situations, the extent of possible radiation damage of phosphor light generating capabilities, and the quantitative difference in light output made by active mixing of the radionuclide and phosphor. However, at a practical level, all of the necessary building blocks for a relatively stable IMD power source are present, most prominently including the potential for more than 100 nW of power over multiple months, as well as a clear strategy for safely enclosing the fuel (specifically, by using a solid, transparent enclosure).

To ensure the practical applicability of this power source for mm-scale IMDs, the radionuclide and phosphor mixture should take up a volume no larger than around 10 mm³, with 1 mm \times 1 mm \times 5 mm being the dimensions of a typical fiducial marker used in radiation therapy (representing a volume of 5 mm³) [22]. As established before, thorium nitrate itself occupies a negligible volume, so evaporation of any mixture of Th-227 with the

phosphor will ensure that the radionuclide does not place a limit on the achievable volume of the system. The volumetric density of the SA-YO phosphor was found empirically to be about $0.7 \mu\text{L}/\text{mg}$ (noting that $1 \mu\text{L}$ is equivalent to 1mm^3). As a result, the practical limit on the amount of SA-YO phosphor that can be used within an IMD similar in size to a fiducial marker for radiation therapy is about 6 mg.

To combine the radionuclide and phosphor to optimally generate light in such a small form factor, a clear capsule, open on one end, could be iteratively filled with a thin layer of phosphor and a set volume of radionuclide solution, before being evaporated. After completely filling the capsule with the radionuclide and phosphor, the capsule would then have its open end sealed with a transparent epoxy or other easily-cured sealant. This strategy would ensure relatively close packing of the radionuclide and phosphor without introducing the need for active mixing and would ensure compatibility with an automated assembly process. The remainder of the system design considerations are discussed in the following chapter, with various approaches for converting the optical energy produced by this source to useful electrical energy for a sensor or other electronic system analyzed.

Chapter 4

Harvester Design Considerations

4.1 Packaging

In order to ensure simple system-level integration and prevent semiconductor radiation damage, it is beneficial to seal the radionuclide-phosphor mixture within some sort of optically clear enclosure. This also eases the assembly process, and protects against contamination of the external environment by the radionuclide. There are many choices available for the enclosing material: borosilicate glass and any number of clear plastic materials, including acrylic, polystyrene, and other polymers, exhibit $\sim 90\%$ transmission of red light (as emitted by the SA-YO phosphor) and have low densities suitable for implantation. The clarity of the material is of negligible importance; in fact, the light output can become more uniform as a result of scattering within the enclosing material, which makes the design of the photovoltaic system simpler. Square or rectangular tubing of a clear material such as these could be used to form a capsule which would allow for the iterative phosphor and radionuclide deposition process described at the end of the last chapter, in which the enclosing capsule is filled with radionuclide solution after the insertion of a thin layer of phosphor, with more space being made through evaporation.

Photovoltaic (PV) cells would then sandwich the sealed capsule, with reflective material layered along the balance of the capsule exterior to avoid optical power loss. The remainder of the implant system, including the sensor and integrated circuitry for power harvesting, data storage, and communication (interfacing with either a small antenna or piezoelectric transducer), would sit on the side of one PV array. In the best case, the PV array would be fabricated together with this other circuitry in an integrated process, although connections could be from a board containing discrete PV cells to the system ASIC. However, even if the PV array on one side was integrated with the system ASIC, there would remain the problem of connecting the PV array on the opposing side as well.

One solution to address this issue would be to restrict the array of PV cells to just one side of the capsule and extend the reflective material to cover the opposing side. At the cost of some absorption within the reflective layer, as it cannot be made perfect, system

integration would be significantly eased. In addition, the reflection could possibly make the light distribution more uniform, which is beneficial to the photovoltaic system as mentioned earlier.

Finally, the different layers would be adhered to each other using an epoxy applied along the exterior of the stack. The resultant bundle would then be enclosed within a biocompatible metal or polymer package, selected to ensure system longevity and complement the implant communication mode.

4.2 Photovoltaic Structure and Characterization

Discrete vs. Integrated

Of primary practical importance is selecting whether to compose any PV arrays of discrete photodiodes sourced from a commercial vendor and placed on a custom printed circuit board (PCB) or integrate them directly above the integrated circuitry via microfabrication. One appealing aspect of using discrete photodiodes is that the choice of the semiconductor material(s) for the photocurrent-generating junction is no longer process-limited. This allows the selection of photodiodes made from InGaAs, InGaP, and other materials, which could potentially provide electron-hole pair generation efficiency above the approximate 20% limit of Si and better match the emission spectrum of the phosphor in the abstract case (a large difference was not evident around red wavelengths, as would be relevant for the SA-YO phosphor). However, while the discrete method could be cost-effective from the perspective of prototype design, it imparts significant challenges, such as the need for cathode and anode connections that will not be destroyed during the assembly process (i.e., wire-bond connections are effectively off-limits) and the inevitable issue of board area under-utilization contributing to optical power loss. As a result, the integrated method is far more appealing due to its convenience, as the circuitry will need to be fabricated in an integrated fashion anyway. This strategy additionally enables customization in the nature of the connections between individual photodiodes (equivalent to “cells”) in the PV array, which will be discussed next.

Nonuniform Illumination

As identified in Chapter 3, the illumination provided by the radionuclide-phosphor mixture can have a significant directional dependence according to the distribution of the radionuclide and phosphor with respect to each other. The direct consequence of this will be that cells in the PV array can expect to have (possibly significantly) different I-V and P-V (current-voltage and power-voltage) characteristics due to nonuniform irradiation. This complicates the process of designing the photodiode interconnection network, as, while higher voltage can be achieved by connecting individual cells in series, this mandates that these cells source the same (lowest) current, potentially placing one or more cells at a less optimal operating

condition from a power perspective. In contrast, placing cells in parallel fixes their voltage to be the same, allowing cells experiencing greater irradiation to produce more current, in general. To achieve higher PV array output voltage while avoiding the scenario where many cells are connected in series and under-utilized due to nonuniform irradiation, one strategy is to connect cells in series with the cells surrounding them to form PV blocks, before connecting those blocks in parallel. This allows the current within each block to match the irradiation conditions local to it, while still allowing for a higher output voltage. Similar approaches have been employed successfully in thermophotovoltaic and solar cell applications suffering from nonuniform irradiation problems as well [32].

Characterization

Photodiode I-V and P-V characteristics are illustrated graphically in Figures 4.1 and 4.2. The general photodiode I-V curve represents a modification to the typical diode I-V curve, where a photocurrent proportional to the amount of incident light is induced in the “reverse” direction. For characterization purposes, the definition of the direction of current flow is flipped to reflect the intended operation of the device. Finally, the P-V curve for a given illumination condition can be generated by simply multiplying the current by the voltage at each point. This curve then provides the maximum power point (MPP), which can then be located on the original I-V curve as well.

PV array optical performance will be evaluated in this fashion before and after system assembly. Block pinouts from the chip will allow testing of the I-V characteristics of individual PV blocks with the remainder of the circuits disabled. This can be achieved by varying the load of each block between 0 and $\infty \Omega$ (open circuit) using a source measure unit (SMU) and measuring the voltage across the block with the same unit or a separate voltmeter. Before assembly, the array will be illuminated by a controlled red light source of similar power to that produced by the radionuclide-phosphor mixture (hundreds of nW to μW), and I-V curves will be generated under these conditions. After assembly and the addition of the radionuclide-phosphor capsule, I-V curves can be measured directly, as the capsule will act as the light source. This process, especially before assembly, will confirm the design parameters for the harvester system. Evaluation following assembly should ideally confirm the pre-assembly characterization, while identifying any nonuniform illumination conditions.

4.3 Power Harvesting Strategies

Given that the process of converting incident radiation into useful electron-hole pairs through a photovoltaic is typically incredibly inefficient itself (an electron-hole pair generation efficiency of approximately 20% is high for Si), it is of paramount importance that the electrical energy harvesting system is as efficient as possible.

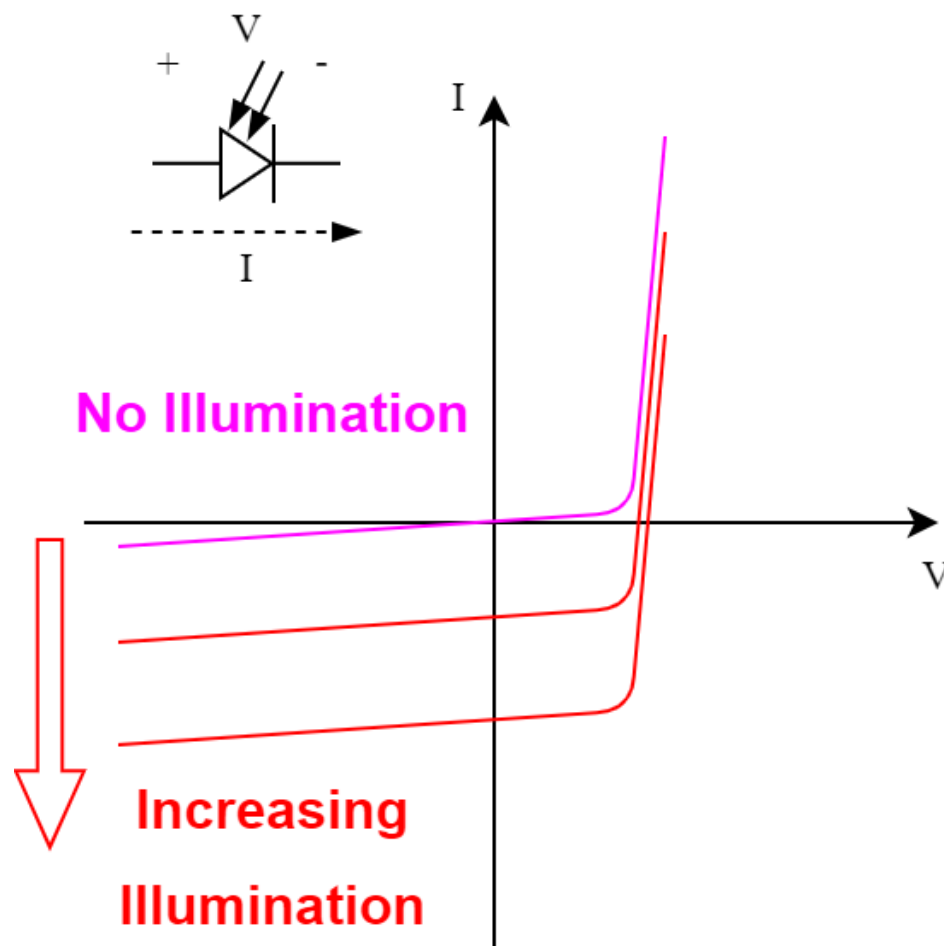


Figure 4.1: Increasing illumination of the photodiode lowers its I-V curve, as the photocurrent travels in the direction opposite the nominal “forward” current.

Driving the Load Directly

The most natural first proposition for delivering the power from a PV system to any given load would be to connect enough of the PV cells in series to match the voltage requirements of the load and drive it directly from that. In practice, a capacitor is necessary to stabilize the load voltage and augment the the current that can be delivered to the load, and this is especially important given the low output current and power of the PV structure.

This strategy is depicted in Figure 4.3, in which a series connection of PV blocks is established to satisfy the voltage requirement of the load. The main advantage of this setup is that there is no conversion loss whatsoever (outside of wiring conduction loss), as no converter is present in the first place! However, the maximum power point of the system is

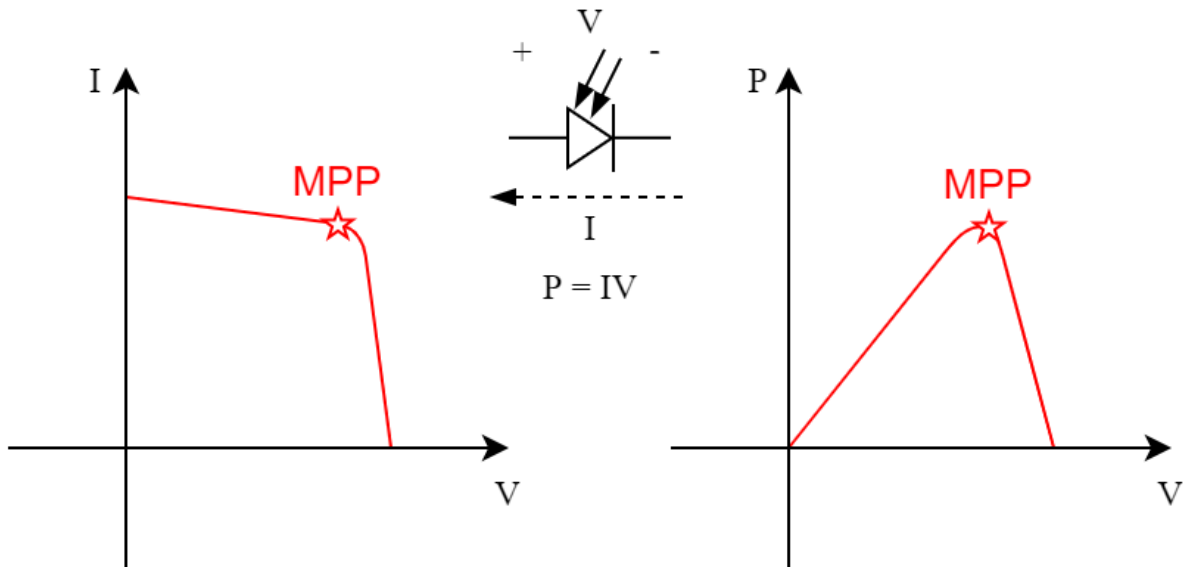


Figure 4.2: Identifying the photocurrent as the relevant energy-generating current, the nominal current direction is flipped and the I-V curve is re-examined for positive voltage and positive current (i.e., positive power delivered to the load). Since $P = IV$, a P-V curve can be derived directly from this new I-V curve, and the maximum power point (MPP) can be located.

almost certainly not reached. Although the current at the block level might be relatively matched, a series connection of blocks with possibly highly diverse current conditions would necessitate that all blocks source the same (lowest) current, rendering the block localization useless. The net effect of this is that the source efficiency falls relatively far below the $>90\%$ achievable with active maximum power point tracking (MPPT), as would typically be implemented with a converter. In a typical case without too much nonuniformity in the irradiation of the cells, this would leave the source efficiency (and overall efficiency) around something like 70% , as a very rough estimate. However, in the worst case that one cell is sourcing significantly less current than the rest, the actual efficiency would fall far below this value.

Ideally, given enough blocks, the interconnection of the blocks would be made somewhat adaptive to variable illumination conditions to reduce this effect. One distinct benefit of the fixed nature of the irradiation in this application is that the relative intensities of the light incident on the different cells do not change to exceed or fall below each other, even if the magnitude of the irradiation is indeed time-varying. As a result, any calibration of the PV interconnection yielding power harvesting near the MPP prior to implantation would continue to produce close to optimal harvesting across the lifetime of the implant. One example of a PV structure with an adaptive, modular interconnection network is depicted in

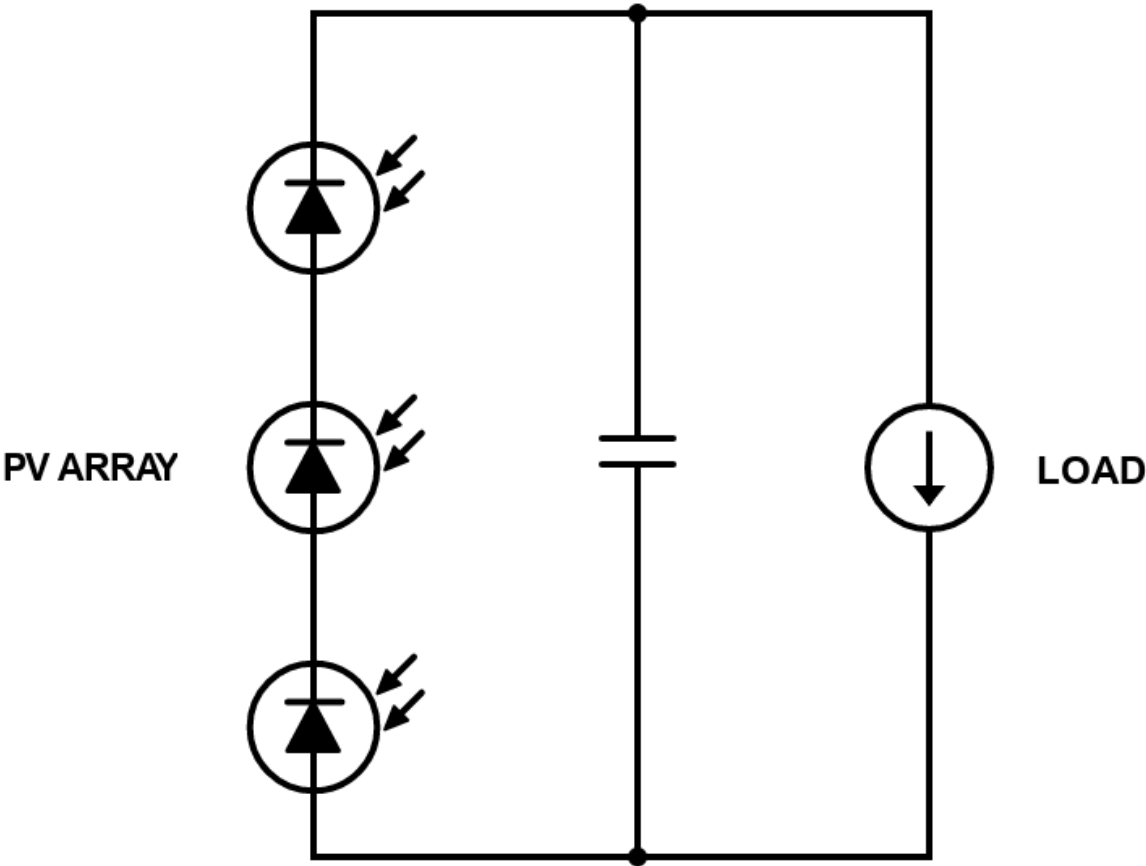


Figure 4.3: The PV blocks are connected in a fixed manner in order to ensure that the voltage requirement of the load is satisfied (only three are shown here, but it more are likely to be necessary in practice). Additional parallel connections are possible for “excess” PV blocks to boost current; however, the total current through the structure will be limited by the lowest current sourced from any stage.

Figure 4.4. In this structure, adjacent blocks can be placed in series or parallel with respect to each other, allowing a broad range of connection possibilities at the cost of the addition of three switches per block. The switch settings producing the most power would be identified and selected through an optimization loop managed by an external controller, which would perform I-V characterization for each collection of settings. The voltage requirement at the load would provide an additional constraint, with some margin on that voltage necessary to account for decay. Such a structure would effectively “bake” MPPT into the device, allowing more optimal power harvesting without significant conversion loss.

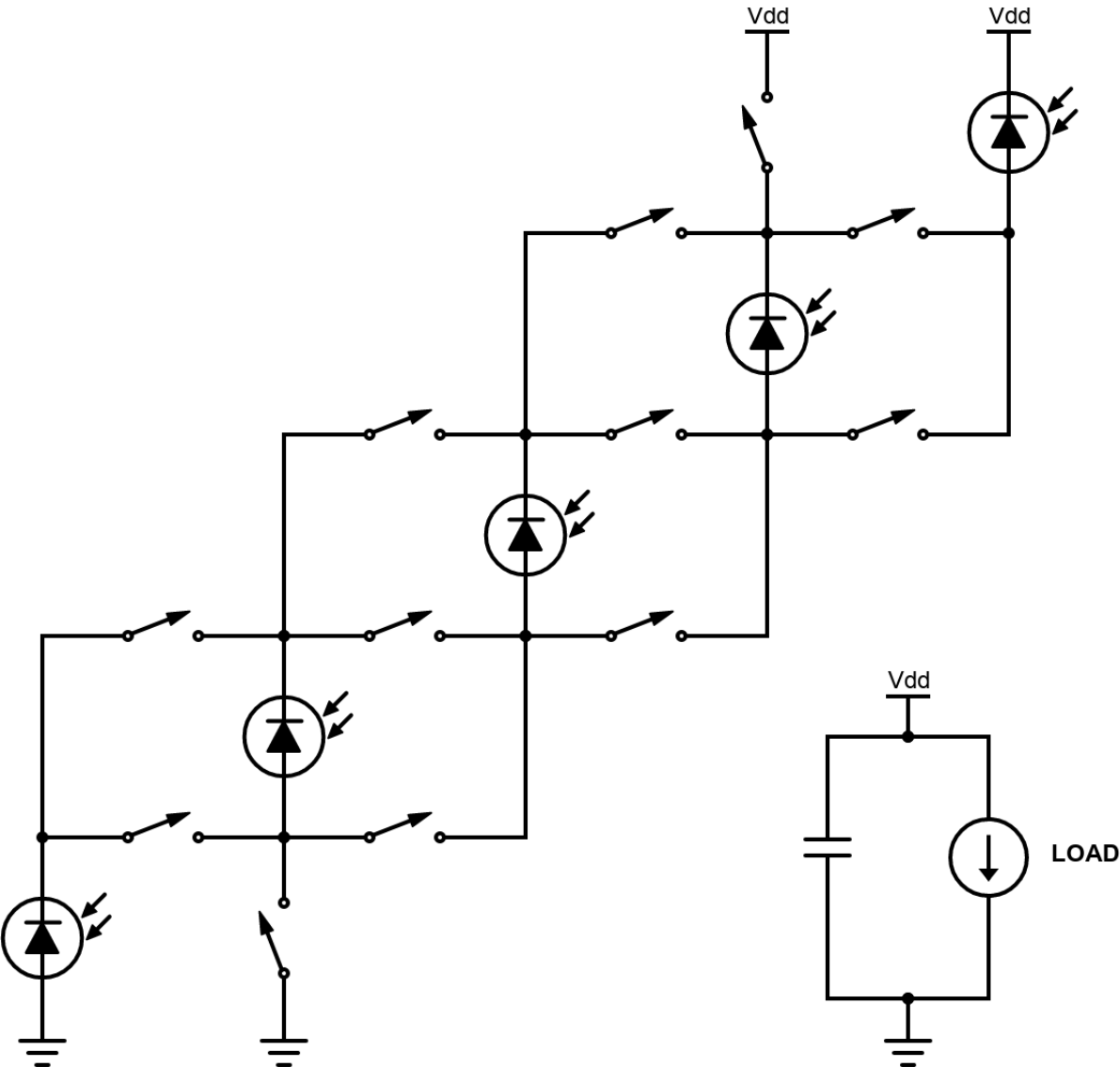


Figure 4.4: Adjacent PV blocks can be connected in series or parallel to maximize source efficiency, with the MPP tracked by the same switch settings across the lifetime of the implant. This optimization can be conducted by an external controller prior to implantation.

Full Step-Up Conversion

If the voltage and current conditions at the source are fixed, a full step-up conversion is often necessary to meet the voltage and current requirements at the load, with the voltage at the load typically being many times that at the source in such cases. This type of design

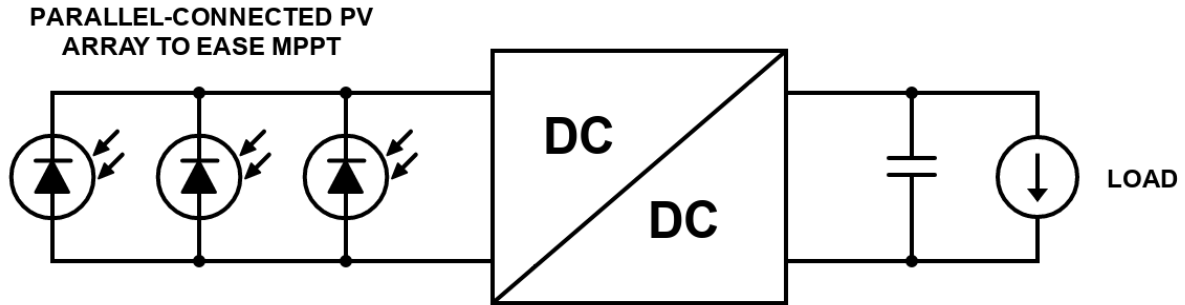


Figure 4.5: With active conversion, MPPT can be implemented through the voltage step-up ratio between the output and input. To ease this, PV blocks at the source are connected in parallel.

is depicted in Figure 4.5, where the voltage at the input of the power converter is kept fixed across the PV blocks by the parallel connection, which allows the current through each block to better approximate the MPP current, since the current varies relatively little around the MPP.

Boost Converter

The design presented in [5] is a good example of a standard inductive boost converter operating at very low power. In this application, the source is the endocochlear potential present in the mammalian ear, which provides a useful input voltage of around 30 to 55 mV [5]. In order to power a typical ASIC from this source, the voltage must be boosted to around 0.8 to 1.1 V, representing a 37-fold increase in the worst case [5]. A switched-inductive power converter such as the boost architecture presented in this paper can be appealing in these circumstances and in general because the voltage conversion ratio is relatively simply predicted for continuous operation from the switching frequency, shunt switch on-period, and boosting inductance value. In discontinuous conduction mode (DCM), which is necessary for low power operation, the load impedance must be included in the calculation as well, and the exact modeling becomes more complicated, but the conversion ratio can still be tuned through the switching duty cycle, defined as the product of the shunt switch on-period and the switching frequency. As a result, if the input voltage varied with time (which it doesn't in the specific application explored in this paper), an MPPT feedback loop could be implemented relatively simply through this switching duty cycle parameter.

Usually, an inductive converter is limited mainly by conduction and switching loss [5], which allows very high efficiency to be attained when these loss modes are relatively negligible compared to the power levels that are being transferred. Unfortunately, this is not the case at nW-levels and below, and other loss modes become important to consider as well, such as

transistor leakage and the switching of parasitic capacitances [5]. As a result, the end-to-end energy conversion efficiency reported in this work is 53% at 1.2 nW of input power [5], which is lower than for boost converters operating at more typical conditions, but comparable or higher than the switched-capacitor converters that will be discussed next. However, the main limiting factor for any inductive power converter potentially being used within a mm-scale IMD is that inductors simply cannot be made this small while also ensuring reasonable efficiency at low power. In this paper, as an example, a 47 μH inductor that is 4.8 mm \times 4.8 mm \times 1.8 mm is used [5]. Therefore, inductive power converters are generally not feasible for truly mm-scale IMD designs.

Switched-Capacitor Converter

As an alternative, a relatively efficient switched-capacitor power harvester is presented in [58] which harvests energy over a wide range ($>40\%$ efficiency between 113 pW and 1.5 μW of input power) by implementing discontinuous conduction at lower power levels. Charge is transferred to the load through a programmable switched-capacitor charge pump which achieves higher conversion ratios by multiplexing the output of an initial charge pump stage into a final series parallel summing stage [58]. As the targeted application for this work is low-illuminance solar cell power harvesting and the input power level is highly variable, active MPPT is implemented through automatic modulation of the charge pump conversion ratio, ensuring proper matching between the load (a battery operating at around 4 V) and the input (around 0.3 V) [58].

Most importantly, this sort of converter can be integrated completely onto a chip, making it feasible for a mm-scale IMD design. However, while this design avoids the miniaturization issues faced by inductive designs, it is highly complex and has been distinctly optimized for 100 nW of input power, where it exhibits its maximum end-to-end efficiency of approximately 55% [58].

In all, the relatively low end-to-end efficiency that can be achieved with a strategy based on full step-up conversion makes this strategy relatively unattractive compared to the methods eschewing active conversion that were discussed previously. The relative simplicity of the direct approach also makes it far more appealing when contrasted with the intense design optimization needed to achieve $<60\%$ end-to-end energy conversion efficiency with a switched-capacitor power converter.

Partial Power Processing

One last approach is that of partial, rather than full, power processing. In this approach, the energy source is provided with a direct path for transferring power to the load, while one or more power converters process power in a “partial” or “differential” sense in order to control the load conditions and perform MPPT. An example of this strategy is shown in Figure 4.6. The partial power processing method is especially applicable in typical solar cell applications where partial shading and nonuniform irradiation are sizeable problems, and

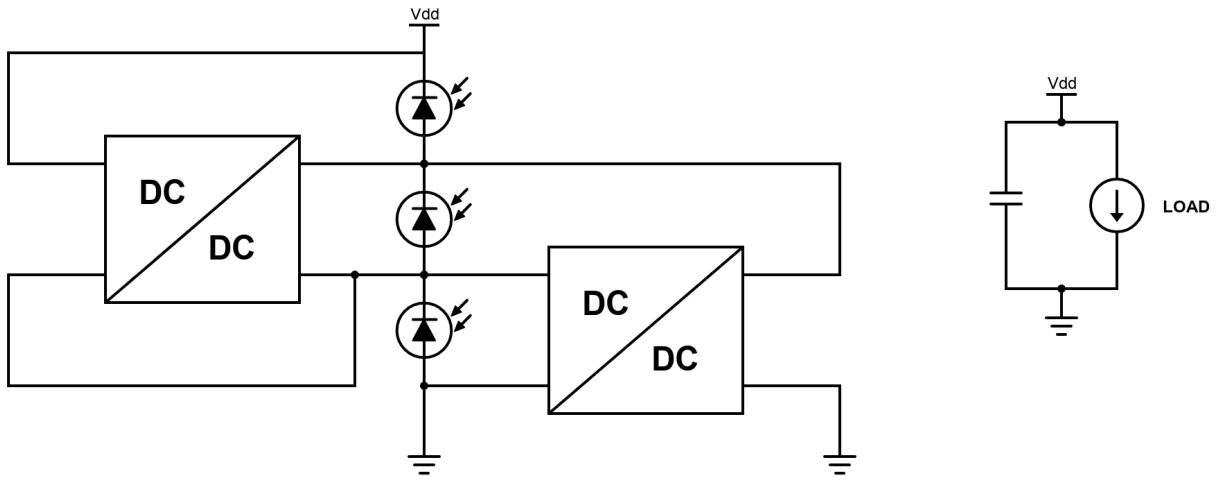


Figure 4.6: Partial or differential power processing can be used to set the conditions at the load and perform MPPT, in addition to reducing conversion loss compared to the case where all of the harvested power is processed through a converter (primarily through the fact that less power is processed through converters to begin with). In this example, each PV block has a direct conduction path to the load, but is placed at its MPP by the auxiliary power converters [35].

where inductive converters normally find use [35]. Because the dominant loss mechanism in inductive converters at higher powers is conduction loss, having each converter simply handle less power, as is the case when each converter is only processing a partial voltage step-up, can noticeably increase conversion efficiency. This is in keeping with the conventional wisdom that efficiency is optimized when the voltage at the input and output of a converter are most closely matched.

However, this approach encounters a few issues at low power levels. For one, the assumption that converter efficiency will necessarily improve through reduction of the power to be processed seems to be unfounded in almost every case. In particular, this appears to be due to the increasing relative magnitude of leakage and parasitic loss, as well as of the power drawn for necessary timing and control circuitry, as input power decreases. In addition, the potential need for multiple converters is particularly unattractive from a miniaturization perspective.

It should be noted that the design depicted in Figure 4.6 is only one possibility. It is also possible to only perform power conversion over select PV blocks, so as to reduce the number of converters in the design (all the way down to one). This would allow for improved end-to-end efficiency compared to the full step-up conversion approach, as a direct power transfer path to the output would be established, while also providing an avenue for some form of active MPPT. Be that as it may, it appears that any strategy making use of

active power conversion at nW-level powers will need to address, in one form or another, the fundamental challenge of converter efficiency decreasing with decreasing input power. As a result, a direct power transfer approach, especially one implementing some form of MPPT, such as the adaptive design proposed previously, might still be the best option from almost every perspective.

4.4 Sensor Integration

To demonstrate complete system integration, the eventual aim is to include an imaging sensor as the “load” for the power source and harvesting system. The requirements for this module, designed within the Anwar research group by Rozhan Rabbani, are specified in Table 4.1.

Table 4.1: Imaging sensor operating requirements.

Specification	Value
Nominal operating voltage	5 V
Minimum operating voltage	3.5 V
Laser current draw	37 mA
Imaging duration	100 ms
Number of laser pulses	50000
Laser pulse duty cycle	50%
Pixel array size	36×40
ADC	8-bit SAR
ADC clock	1 MHz

Load Capacitance

First, the current draw of the module provides information on the energy storage and current-boosting capacitance required at the load of the harvesting system.

$$I = C \frac{dV}{dt} \Rightarrow (0.5) \cdot (37 \text{ mA}) = C \cdot \frac{5 \text{ V} - 3.5 \text{ V}}{100 \text{ ms}} \quad (4.1)$$

This yields that at least 1.233 mF of capacitance is required to support the current demands of this imager. This places an immediate block on miniaturization, since such a large capacitance can only be implemented practically at a small scale through the parallel connection of smaller capacitances. At best, these smaller capacitances will be housed in mm-scale packages themselves, so the entire system is limited to having at least one dimension extend over a centimeter or more. However, research is ongoing on reducing the imager peak

current draw by using an LED rather than a laser diode. If this could be reduced to about 1 mA, the capacitance requirement would drop to about 33 μF , which is far more achievable at mm-scale.

Energy

Perhaps more fundamental is the calculation of the energy required for this sensor to take a measurement.

$$P_{min} = I \cdot V_{min} = (0.5) \cdot (37 \text{ mA}) \cdot (3.5 \text{ V}) = 64.75 \text{ mW} \quad (4.2)$$

$$E_{min} = P_{min}T = (64.75 \text{ mW}) \cdot (100 \text{ ms}) = 6.475 \text{ mJ} \quad (4.3)$$

With, say, 100 nW of power provided by the harvesting system to the load capacitor, this implies that measurements could theoretically be taken by this sensor every 18 hours. Although the optimal combination of radionuclide and phosphor has not been specifically identified just yet, an output power of 100 nW over the course of three months or more is a realistically achievable target, as with a total optical-to-electrical harvesting efficiency of 10% (assuming, say, 20% electron-hole pair generation efficiency and 50% harvester efficiency), this would require 1 μW of optical power to be generated by the mixture. Of course, with a more efficient harvester, this requirement becomes significantly relaxed as well.

It is also worth noting that this sensor is about as energy-demanding as implantable sensors are likely to get. With just the aforementioned current reduction to 1 mA, 100 nW of harvester output power would enable a measurement every 30 minutes, or, conversely, allocating 18 hours to charge the load capacitor would require only 2.7 nW to be delivered to charge it. For more energy-efficient sensors, nW-levels of power are more than sufficient to allow robust, relatively high-frequency operation.

Data Storage and Communication

Allowing data to be collected independently and interrogated on demand by an external agent is one of the greatest benefits that the use of independent power on an implant can provide, as current strategies which are dependent on power that is beamed-in require that the implant be interrogated in order for measurements to be taken.

On this sensor, there is a total of 1440 pixels, with 8 bits read out serially per pixel from the on-chip ADC. As a result, each frame contains 11520 bits (or 1440 8-bit words) of information, which is just under 1.5 kB. It is therefore eminently feasible to include static random-access memory (SRAM), or even some form of non-volatile memory (NVM), to store multiple images on the harvester chip, with only minor modifications necessary to ensure that data can be read-in and stored properly.

Data communication can be achieved through the RF or US modalities. For RF communication, ultra-wideband (UWB) pulses can enable high-bandwidth ($\sim\text{Mbps}$), low-power communication, with per-pulse energy dissipation demonstrated to be on the order of tens of

pJ or less in an implantable context [7, 38]. As explored heavily in the literature, the communication link between an IMD and any external receiver is a highly asymmetric one that greatly incentivizes simplifications to the transmitter design at the cost of complication in the design of the external receiver, as the transmitter is intensely space- and power-constrained, while the receiver has almost no such limitations [7, 38]. Due to the relatively significant attenuation experienced by EM waves in the human body, this link asymmetry is particularly salient with regards to RF communication system design within the body. As a result, a significant amount of design effort is required to integrate and optimize an mm-scale (or smaller) antenna and RF transmitter with the IMD ASIC, in addition to verifying communication through a tissue model [7]. In contrast, the most prominent design optimization possibly required on the side of the external receiver is in the specific dimensions and loop structure of the antenna, with comparatively minimal constraints to size or power [7].

The main benefit of choosing the US modality over the RF modality is that ultrasound's greatly reduced path loss through tissue significantly eases the design of the transmitter on the side of the implant [44]. In addition, digital communication, which is inherently resistant to noise and interference, is preferred in US-based systems. Specifically, the on-off keying (OOK) and amplitude-shift keying (ASK) schemes can be used in this context [30, 49], with the load of the implant piezoelectric transducer varying in quantized steps so as to change the transducer reflectivity accordingly. This produces quantized steps in the wave backscattered by the transducer in response to an incident US beam sourced from the interrogator. The backscattered wave is then received and processed by the interrogator in turn, with data rates on the order of kbps attainable. The transmitters for these digital schemes are fairly straightforward to implement, as described in Chapter 1, with one or more FETs connected in parallel to the transducer being switched "on" or "off" to set the load impedance according to the desired modulation.

As a result, the implant piezoelectric transducer would need only to be designed to reflect a signal strong enough to be received accurately at the interrogator. This would allow significant miniaturization over most of the designs currently found in the literature, which rely on the transducer to receive power as well and therefore require it to be larger (around 1 mm^3). The core limitation to this approach compared to that of using RF communication is that the transducer simply cannot be integrated with the IMD ASIC. However, the corresponding size penalty is potentially justified in certain physiological contexts that are prohibitive to the use of RF communication.

Chapter 5

Conclusion

5.1 Next Steps

As elucidated near the close of Chapter 3, it is necessary to identify the most optimal practical combination of the preferred SA-YO phosphor with Th-227 to establish a clear path for use of these materials as an energy source for an IMD system. Of primary concern in this case is ensuring that the radionuclide-phosphor mixture occupies a volume that will allow the implant in its entirety to resemble the form factor of a fiducial marker used in radiation therapy ($1\text{ mm} \times 1\text{ mm} \times 5\text{ mm}$), while continuing to produce hundreds of nW or more of optical power. This work will begin shortly after the time of writing, and should reinforce the findings presented here. Practical measures will be taken to avoid some of the issues encountered during the last experiment, including the use of centrifuge tubes with snap-on caps and conical ends to ease the evaporation process and ensure that the entire mixture is localized to a small volume within each container.

Once this step is completed, the work of integrating this energy source with a harvester system with sensing and communication capabilities can be undertaken, as outlined in Chapter 4. The harvester itself would be verified to operate correctly when exposed to a similar amount of light in a controlled laboratory environment before being added to the packaging of the energy source and verified in that context as well. Finally, any sensing and communication capabilities would be tested *in vitro*, with *in vivo* experiments to follow.

5.2 Outlook

This work has demonstrated that the combination of a radionuclide with a phosphorescent material can produce enough power to enable independent mm-scale implanted wireless sensing over months and even years, greatly accelerating the therapeutic feedback loop for a diverse range of applications. Critically, this solution will at once improve the quality and quantity of the diagnostic information available to care providers, while at the same time allowing care to become more convenient for the patient and those that care for them.

This radionuclide-based approach has been explored to provide an immediate path toward this new paradigm, but, hopefully, additional paths will make themselves apparent in the near future. Of note in particular is the rapidly-improving state of battery technology at mm-scale, which seems almost certain to provide a path to independent IMD power over a lifetime of a few months (at least) in the years to come. The main limiter in the case of batteries seems to be their self-discharge characteristics, with additional study required in implanted conditions, where higher temperatures could adversely affect performance, among other considerations. For rechargeable batteries, however, one straightforward method for ensuring system longevity would be to integrate power harvesting through US or EM with the interrogation necessary for data collection. Although this would not necessarily allow the scaling promised by a truly long-lasting independent miniature power source, it would at least directly address the energy storage problem faced by modern wireless power strategies for IMDs.

Furthermore, there exists the possibility of augmenting the capabilities of a radionuclide-based system with a miniature battery as the main energy storage module at the load. With a radionuclide like Th-227, which can certainly provide power over many months but sees a drop-off beyond that timescale, such an addition would effectively allow the radionuclide, which produces the most power immediately following implantation, to provide all or most of the power required by the sensing and communication systems during this period. Since the diagnostic information provided by the sensor would be especially crucial at this point — more or less directly setting the prognosis — the sensor could be operated more frequently. As the power from the radionuclide source would naturally ebb, the battery would incrementally “take over”, with the overall lifetime of the combined power source likely far exceeding that capable by just one or the other by itself.

The potential of this combined approach, as well as that of simply using a radionuclide with a longer half-life (with an accordingly higher activity), bodes well for the prospects of the system proposed here, as well as implanted diagnostic sensing in general.

Bibliography

- [1] Suhaib Ahmed and Vipin Kakkar. “An Electret-Based Angular Electrostatic Energy Harvester for Battery-Less Cardiac and Neural Implants”. In: *IEEE Access* 5 (2017). Conference Name: IEEE Access, pp. 19631–19643. ISSN: 2169-3536. DOI: [10.1109/ACCESS.2017.2739205](https://doi.org/10.1109/ACCESS.2017.2739205).
- [2] Georgios Arnaoutakis. “Characterisation of Up-conversion in Rare-earth Materials”. In: *Edinburgh Instruments Application Notes* (), p. 6. URL: https://www.edinst.com/wp-content/uploads/2018/03/Characterisation-on-Up-conversion-in-Rare-earth-Materials_ForWeb.pdf.
- [3] Frank Herbert Attix. “Radioactive Decay”. In: *Introduction to Radiological Physics and Radiation Dosimetry*. Section: 6. John Wiley & Sons, Ltd, 1986, pp. 101–123. ISBN: 978-3-527-61713-5. DOI: [10.1002/9783527617135.ch6](https://doi.org/10.1002/9783527617135.ch6). URL: <https://onlinelibrary.wiley.com/doi/abs/10.1002/9783527617135.ch6> (visited on 04/30/2021).
- [4] S.G. Bailey et al. “Photovoltaic development for alpha voltaic batteries”. In: *Conference Record of the Thirty-first IEEE Photovoltaic Specialists Conference, 2005*. Conference Record of the Thirty-first IEEE Photovoltaic Specialists Conference, 2005. ISSN: 0160-8371. Jan. 2005, pp. 106–109. DOI: [10.1109/PVSC.2005.1488080](https://doi.org/10.1109/PVSC.2005.1488080).
- [5] Saurav Bandyopadhyay et al. “A 1.1 nW Energy-Harvesting System with 544 pW Quiescent Power for Next-Generation Implants”. In: *IEEE Journal of Solid-State Circuits* 49.12 (Dec. 2014). Conference Name: IEEE Journal of Solid-State Circuits, pp. 2812–2824. ISSN: 1558-173X. DOI: [10.1109/JSSC.2014.2350260](https://doi.org/10.1109/JSSC.2014.2350260).
- [6] Hervasio G. de Carvalho and Herman Yagoda. “The Range of Alpha-Particles in Water”. In: *Physical Review* 88.2 (Oct. 15, 1952). Publisher: American Physical Society, pp. 273–278. DOI: [10.1103/PhysRev.88.273](https://doi.org/10.1103/PhysRev.88.273). URL: <https://link.aps.org/doi/10.1103/PhysRev.88.273> (visited on 04/30/2021).
- [7] Jayant Charthad et al. “A mm-Sized Implantable Medical Device (IMD) With Ultrasonic Power Transfer and a Hybrid Bi-Directional Data Link”. In: *IEEE Journal of Solid-State Circuits* 50.8 (Aug. 2015). Conference Name: IEEE Journal of Solid-State Circuits, pp. 1741–1753. ISSN: 1558-173X. DOI: [10.1109/JSSC.2015.2427336](https://doi.org/10.1109/JSSC.2015.2427336).

- [8] Cory D. Cress et al. “Quantum dot solar cell tolerance to alpha-particle irradiation”. In: *Applied Physics Letters* 91.18 (Oct. 29, 2007). Publisher: American Institute of Physics, p. 183108. ISSN: 0003-6951. DOI: [10.1063/1.2803854](https://doi.org/10.1063/1.2803854). URL: <https://aip.scitation.org/doi/10.1063/1.2803854> (visited on 04/30/2021).
- [9] *Cymbet Corporation EnerChip (TM) Bare Die Rechargeable Solid State Bare Die Batteries*. URL: <https://www.cymbet.com/wp-content/uploads/2019/02/DS-72-41-v6.pdf> (visited on 04/26/2021).
- [10] A. Datas and A. Martí. “Thermophotovoltaic energy in space applications: Review and future potential”. In: *Solar Energy Materials and Solar Cells* 161 (Mar. 1, 2017), pp. 285–296. ISSN: 0927-0248. DOI: [10.1016/j.solmat.2016.12.007](https://doi.org/10.1016/j.solmat.2016.12.007). URL: <https://www.sciencedirect.com/science/article/pii/S0927024816305281> (visited on 04/27/2021).
- [11] M. Deterre et al. “Micromachined piezoelectric spirals and ultra-compliant packaging for blood pressure energy harvesters powering medical implants”. In: *2013 IEEE 26th International Conference on Micro Electro Mechanical Systems (MEMS)*. 2013 IEEE 26th International Conference on Micro Electro Mechanical Systems (MEMS). ISSN: 1084-6999. Jan. 2013, pp. 249–252. DOI: [10.1109/MEMSYS.2013.6474224](https://doi.org/10.1109/MEMSYS.2013.6474224).
- [12] *Front Edge Technology Technical Information*. URL: <http://frontedgetechnology.com/tech.htm> (visited on 04/26/2021).
- [13] Maurice M. Garcia et al. “Endoscopic Gold Fiducial Marker Placement into the Bladder Wall to Optimize Radiotherapy Targeting for Bladder-Preserving Management of Muscle-Invasive Bladder Cancer: Feasibility and Initial Outcomes”. In: *PLOS ONE* 9.3 (Mar. 3, 2014). Publisher: Public Library of Science, e89754. ISSN: 1932-6203. DOI: [10.1371/journal.pone.0089754](https://doi.org/10.1371/journal.pone.0089754). URL: <https://journals.plos.org/plosone/article?id=10.1371/journal.pone.0089754> (visited on 04/27/2021).
- [14] W. A. Herrmann and Frank T. Edelmann. *Synthetic Methods of Organometallic and Inorganic Chemistry, Volume 6, 1997: Volume 6: Lanthanides and Actinides*. Google-Books-ID: oYyZAwAAQBAJ. Georg Thieme Verlag, May 14, 2014. 337 pp. ISBN: 978-3-13-179461-1.
- [15] Helen Heyerdahl et al. “Targeted Alpha Therapy with ^{227}Th -trastuzumab of Intraperitoneal Ovarian Cancer in Nude Mice”. In: *Current Radiopharmaceuticals* 6.2 (May 31, 2013), pp. 106–116. URL: <https://www.eurekaselect.com/111983/article> (visited on 04/30/2021).
- [16] John S. Ho et al. “Wireless power transfer to deep-tissue microimplants”. In: *Proceedings of the National Academy of Sciences* 111.22 (June 3, 2014). Publisher: National Academy of Sciences Section: Physical Sciences, pp. 7974–7979. ISSN: 0027-8424, 1091-6490. DOI: [10.1073/pnas.1403002111](https://doi.org/10.1073/pnas.1403002111). URL: <https://www.pnas.org/content/111/22/7974> (visited on 04/28/2021).

- [17] Leigh R. Hochberg et al. “Reach and grasp by people with tetraplegia using a neurally controlled robotic arm”. In: *Nature* 485.7398 (May 2012). Number: 7398 Publisher: Nature Publishing Group, pp. 372–375. ISSN: 1476-4687. DOI: [10.1038/nature11076](https://doi.org/10.1038/nature11076). URL: <https://www.nature.com/articles/nature11076> (visited on 04/27/2021).
- [18] Seth Hubbard et al. “Nanostructured photovoltaics for space power”. In: *Journal of Nanophotonics* 3.1 (Oct. 2009). Publisher: International Society for Optics and Photonics, p. 031880. ISSN: 1934-2608, 1934-2608. DOI: [10.1117/1.3266502](https://doi.org/10.1117/1.3266502). URL: <https://www.spiedigitallibrary.org/journals/journal-of-nanophotonics/volume-3/issue-1/031880/Nanostructured-photovoltaics-for-space-power/10.1117/1.3266502.short> (visited on 04/27/2021).
- [19] *IVIS 50 Hardware Manual*. Nov. 2002.
- [20] S. Kerzenmacher et al. “An abiotically catalyzed glucose fuel cell for powering medical implants: Reconstructed manufacturing protocol and analysis of performance”. In: *Journal of Power Sources* 182.1 (July 15, 2008), pp. 66–75. ISSN: 0378-7753. DOI: [10.1016/j.jpowsour.2008.03.049](https://doi.org/10.1016/j.jpowsour.2008.03.049). URL: <https://www.sciencedirect.com/science/article/pii/S0378775308006149> (visited on 04/27/2021).
- [21] Gerasimos Konstantatos and Edward H. Sargent. “Colloidal quantum dot photodetectors”. In: *Infrared Physics & Technology*. Proceedings of the International Conference on Quantum Structure Infrared Photodetector (QSIP) 2010 54.3 (May 1, 2011), pp. 278–282. ISSN: 1350-4495. DOI: [10.1016/j.infrared.2010.12.029](https://doi.org/10.1016/j.infrared.2010.12.029). URL: <https://www.sciencedirect.com/science/article/pii/S1350449510001301> (visited on 04/30/2021).
- [22] Nishita Kothary et al. “Safety and Efficacy of Percutaneous Fiducial Marker Implantation for Image-guided Radiation Therapy”. In: *Journal of Vascular and Interventional Radiology* 20.2 (Feb. 1, 2009), pp. 235–239. ISSN: 1051-0443. DOI: [10.1016/j.jvir.2008.09.026](https://doi.org/10.1016/j.jvir.2008.09.026). URL: <https://www.sciencedirect.com/science/article/pii/S105104430800883X> (visited on 04/27/2021).
- [23] Geoffrey A. Landis et al. “Non-solar photovoltaics for small space missions”. In: *2012 38th IEEE Photovoltaic Specialists Conference*. 2012 38th IEEE Photovoltaic Specialists Conference. ISSN: 0160-8371. June 2012, pp. 002819–002824. DOI: [10.1109/PVSC.2012.6318178](https://doi.org/10.1109/PVSC.2012.6318178).
- [24] S. E. Létant and T.-F. Wang. “Semiconductor Quantum Dot Scintillation under -Ray Irradiation”. In: *Nano Letters* 6.12 (Dec. 1, 2006). Publisher: American Chemical Society, pp. 2877–2880. ISSN: 1530-6984. DOI: [10.1021/nl0620942](https://doi.org/10.1021/nl0620942). URL: <https://doi.org/10.1021/nl0620942> (visited on 04/30/2021).
- [25] S. E. Létant and T.-F. Wang. “Study of porous glass doped with quantum dots or laser dyes under alpha irradiation”. In: *Applied Physics Letters* 88.10 (Mar. 6, 2006). Publisher: American Institute of Physics, p. 103110. ISSN: 0003-6951. DOI: [10.1063/](https://doi.org/10.1063/)

- 1.2182072. URL: <https://aip.scitation.org/doi/10.1063/1.2182072> (visited on 04/30/2021).
- [26] Nicolas Mano. “A 280 W cm² biofuel cell operating at low glucose concentration”. In: *Chemical Communications* 19 (May 8, 2008). Publisher: The Royal Society of Chemistry, pp. 2221–2223. ISSN: 1364-548X. DOI: [10.1039/B801786G](https://pubs.rsc.org/en/content/articlelanding/2008/cc/b801786g). URL: <https://pubs.rsc.org/en/content/articlelanding/2008/cc/b801786g> (visited on 04/28/2021).
- [27] Nirul Masurkar et al. “Millimeter-scale lithium ion battery packaging for high-temperature sensing applications”. In: *Journal of Power Sources* 399 (Sept. 30, 2018), pp. 179–185. ISSN: 0378-7753. DOI: [10.1016/j.jpowsour.2018.07.077](https://www.sciencedirect.com/science/article/pii/S0378775318307948). URL: <https://www.sciencedirect.com/science/article/pii/S0378775318307948> (visited on 04/27/2021).
- [28] Iain Murray et al. “Quantitative Dual-Isotope Planar Imaging of Thorium-227 and Radium-223 Using Defined Energy Windows”. In: *Cancer Biotherapy & Radiopharmaceuticals* 35.7 (Sept. 1, 2020), pp. 530–539. ISSN: 1084-9785. DOI: [10.1089/cbr.2019.3554](https://www.ncbi.nlm.nih.gov/pmc/articles/PMC7475104/). URL: <https://www.ncbi.nlm.nih.gov/pmc/articles/PMC7475104/> (visited on 04/30/2021).
- [29] *Oak Ridge National Laboratory automates key process in plutonium-238 production*. Energy.gov. URL: <https://www.energy.gov/ne/articles/oak-ridge-national-laboratory-automates-key-process-plutonium-238-production> (visited on 04/27/2021).
- [30] Shaul Ozeri and Doron Shmilovitz. “Simultaneous backward data transmission and power harvesting in an ultrasonic transcutaneous energy transfer link employing acoustically dependent electric impedance modulation”. In: *Ultrasonics* 54.7 (Sept. 1, 2014), pp. 1929–1937. ISSN: 0041-624X. DOI: [10.1016/j.ultras.2014.04.019](https://www.sciencedirect.com/science/article/pii/S0041624X14001103). URL: <https://www.sciencedirect.com/science/article/pii/S0041624X14001103> (visited on 06/16/2021).
- [31] David K. Piech et al. “A wireless millimetre-scale implantable neural stimulator with ultrasonically powered bidirectional communication”. In: *Nature Biomedical Engineering* 4.2 (Feb. 2020). Number: 2 Publisher: Nature Publishing Group, pp. 207–222. ISSN: 2157-846X. DOI: [10.1038/s41551-020-0518-9](https://www.nature.com/articles/s41551-020-0518-9). URL: <https://www.nature.com/articles/s41551-020-0518-9> (visited on 04/27/2021).
- [32] Robert C. N. Pilawa-Podgurski et al. “Integrated CMOS Energy Harvesting Converter With Digital Maximum Power Point Tracking for a Portable Thermophotovoltaic Power Generator”. In: *IEEE Journal of Emerging and Selected Topics in Power Electronics* 3.4 (Dec. 2015). Conference Name: IEEE Journal of Emerging and Selected Topics in Power Electronics, pp. 1021–1035. ISSN: 2168-6785. DOI: [10.1109/JESTPE.2015.2470643](https://doi.org/10.1109/JESTPE.2015.2470643).

- [33] *Protecting Against Exposure*. ANS. URL: <http://nuclearconnect.org/know-nuclear/science/protecting> (visited on 04/27/2021).
- [34] David L. Purdy. “Nuclear Batteries for Implantable Applications”. In: *Batteries for Implantable Biomedical Devices*. Ed. by Boone B. Owens. Boston, MA: Springer US, 1986, pp. 285–352. ISBN: 978-1-4684-9045-9. DOI: [10.1007/978-1-4684-9045-9_11](https://doi.org/10.1007/978-1-4684-9045-9_11). URL: https://doi.org/10.1007/978-1-4684-9045-9_11 (visited on 04/27/2021).
- [35] Shibin Qin and Robert C.N. Pilawa-Podgurski. “Sub-module differential power processing for photovoltaic applications”. In: *2013 Twenty-Eighth Annual IEEE Applied Power Electronics Conference and Exposition (APEC)*. 2013 Twenty-Eighth Annual IEEE Applied Power Electronics Conference and Exposition (APEC). ISSN: 1048-2334. Mar. 2013, pp. 101–108. DOI: [10.1109/APEC.2013.6520193](https://doi.org/10.1109/APEC.2013.6520193).
- [36] *QSA-645 - Amine - Functionalized Quantum Dots - Quantum Dots & Quantum Dots Beads - By Products Type*. URL: <https://www.oceannanotech.com/products-type/quantum-dots-quantum-dots-beads/functionalized-quantum-dots/amine-9/qs-a-645.html> (visited on 05/03/2021).
- [37] *QSP-645 - Normal Shipping*. URL: <https://www.oceannanotech.com/by-shipping/normal-shipping/qsp-645.html> (visited on 05/09/2021).
- [38] Jan M. Rabaey et al. “Powering and communicating with mm-size implants”. In: *2011 Design, Automation Test in Europe*. 2011 Design, Automation Test in Europe. ISSN: 1558-1101. Mar. 2011, pp. 1–6. DOI: [10.1109/DATE.2011.5763123](https://doi.org/10.1109/DATE.2011.5763123).
- [39] *Radioactivity : Cherenkov Effect*. URL: https://www.radioactivity.eu.com/site/pages/Cherenkov_Effect.htm (visited on 05/12/2021).
- [40] *Rare earth doped phosphor nanoparticles 900557*. Fluorescent nanoparticles. URL: <https://www.sigmaaldrich.com/catalog/product/aldrich/900557> (visited on 05/09/2021).
- [41] Mahdi Rasouli and Louis Soo Jay Phee. “Energy sources and their development for application in medical devices”. In: *Expert Review of Medical Devices* 7.5 (Sept. 1, 2010). Publisher: Taylor & Francis. eprint: <https://doi.org/10.1586/erd.10.20>, pp. 693–709. ISSN: 1743-4440. DOI: [10.1586/erd.10.20](https://doi.org/10.1586/erd.10.20). URL: <https://doi.org/10.1586/erd.10.20> (visited on 04/27/2021).
- [42] G. Rybicki, C. Vargas-Aburto, and R. Uribe. “Silicon carbide alphavoltaic battery”. In: *Conference Record of the Twenty Fifth IEEE Photovoltaic Specialists Conference - 1996*. Conference Record of the Twenty Fifth IEEE Photovoltaic Specialists Conference - 1996. ISSN: 0160-8371. May 1996, pp. 93–96. DOI: [10.1109/PVSC.1996.563955](https://doi.org/10.1109/PVSC.1996.563955).
- [43] Dongjin Seo et al. “Model validation of untethered, ultrasonic neural dust motes for cortical recording”. In: *Journal of Neuroscience Methods*. Brain Computer Interfaces; Tribute to Greg A. Gerhardt 244 (Apr. 15, 2015), pp. 114–122. ISSN: 0165-0270. DOI: [10.1016/j.jneumeth.2014.07.025](https://doi.org/10.1016/j.jneumeth.2014.07.025). URL: <https://www.sciencedirect.com/science/article/pii/S0165027014002842> (visited on 04/27/2021).

- [44] Dongjin Seo et al. “Neural Dust: An Ultrasonic, Low Power Solution for Chronic Brain-Machine Interfaces”. In: *arXiv:1307.2196 [physics, q-bio]* (July 8, 2013). arXiv: 1307.2196. URL: <http://arxiv.org/abs/1307.2196> (visited on 04/27/2021).
- [45] *SGA 555 100 isiphorjSUPj®j/SUPj 900437*. Yellow phosphor. URL: <https://www.sigmaaldrich.com/catalog/product/aldrich/900437> (visited on 05/09/2021).
- [46] “Shielding Radiation Alphas, Betas, Gammas and Neutrons”. July 5, 2011. URL: <https://www.nrc.gov/docs/ML1122/ML11229A721.pdf>.
- [47] *Sodium yttrium fluoride, ytterbium and erbium doped 756555*. Sigma-Aldrich. URL: <https://www.sigmaaldrich.com/catalog/product/aldrich/756555> (visited on 05/09/2021).
- [48] *Solid angle*. In: *Wikipedia*. Page Version ID: 1020832420. May 1, 2021. URL: https://en.wikipedia.org/w/index.php?title=Solid_angle&oldid=1020832420 (visited on 05/02/2021).
- [49] Soner Sonmezoglu and Michel M. Maharbiz. “34.4 A 4.5mm³ Deep-Tissue Ultrasonic Implantable Luminescence Oxygen Sensor”. In: *2020 IEEE International Solid- State Circuits Conference - (ISSCC)*. 2020 IEEE International Solid- State Circuits Conference - (ISSCC). ISSN: 2376-8606. Feb. 2020, pp. 454–456. DOI: [10.1109/ISSCC19947.2020.9062946](https://doi.org/10.1109/ISSCC19947.2020.9062946).
- [50] M. G. Spencer and T. Alam. “High power direct energy conversion by nuclear batteries”. In: *Applied Physics Reviews* 6.3 (Sept. 1, 2019). Publisher: American Institute of Physics, p. 031305. DOI: [10.1063/1.5123163](https://doi.org/10.1063/1.5123163). URL: <https://aip.scitation.org/doi/10.1063/1.5123163> (visited on 04/27/2021).
- [51] Alok M. Srivastava. “Phosphors”. In: *Encyclopedia of Physical Science and Technology (Third Edition)*. Ed. by Robert A. Meyers. New York: Academic Press, Jan. 1, 2003, pp. 855–872. ISBN: 978-0-12-227410-7. DOI: [10.1016/B0-12-227410-5/00561-5](https://doi.org/10.1016/B0-12-227410-5/00561-5). URL: <https://www.sciencedirect.com/science/article/pii/B0122274105005615> (visited on 05/12/2021).
- [52] Maxim Sychov et al. “Alpha indirect conversion radioisotope power source”. In: *Applied Radiation and Isotopes* 66.2 (Feb. 1, 2008), pp. 173–177. ISSN: 0969-8043. DOI: [10.1016/j.apradiso.2007.09.004](https://doi.org/10.1016/j.apradiso.2007.09.004). URL: <https://www.sciencedirect.com/science/article/pii/S0969804307002771> (visited on 05/20/2021).
- [53] Jonas Thelin et al. “Implant Size and Fixation Mode Strongly Influence Tissue Reactions in the CNS”. In: *PLOS ONE* 6.1 (Jan. 26, 2011). Publisher: Public Library of Science, e16267. ISSN: 1932-6203. DOI: [10.1371/journal.pone.0016267](https://doi.org/10.1371/journal.pone.0016267). URL: <https://journals.plos.org/plosone/article?id=10.1371/journal.pone.0016267> (visited on 04/27/2021).

- [54] Vlado Valković. “CHAPTER 5 - Measurements of Radioactivity”. In: *Radioactivity in the Environment*. Ed. by Vlado Valković. Amsterdam: Elsevier Science, Jan. 1, 2000, pp. 117–258. ISBN: 978-0-444-82954-2. DOI: [10.1016/B978-044482954-2.50005-8](https://doi.org/10.1016/B978-044482954-2.50005-8). URL: <https://www.sciencedirect.com/science/article/pii/B9780444829542500058> (visited on 05/01/2021).
- [55] Ron Walli. *ORNL achieves milestone with plutonium-238 sample*. Oak Ridge National Laboratory Press Release. Dec. 22, 2015. URL: <https://www.ornl.gov/news/ornl-achieves-milestone-plutonium-238-sample> (visited on 04/27/2021).
- [56] Scott A. Whalen, Christopher A. Apblett, and Terrence L. Aselage. “Improving power density and efficiency of miniature radioisotopic thermoelectric generators”. In: *Journal of Power Sources* 180.1 (May 15, 2008), pp. 657–663. ISSN: 0378-7753. DOI: [10.1016/j.jpowsour.2008.01.080](https://doi.org/10.1016/j.jpowsour.2008.01.080). URL: <https://www.sciencedirect.com/science/article/pii/S037877530800205X> (visited on 04/27/2021).
- [57] V. Wood and N. L. Ackerman. “Cherenkov light production from the β -emitting decay chains of ^{223}Ra , ^{212}Pb , and ^{149}Tb for Cherenkov Luminescence Imaging”. In: *Applied Radiation and Isotopes* 118 (Dec. 1, 2016), pp. 354–360. ISSN: 0969-8043. DOI: [10.1016/j.apradiso.2016.10.009](https://doi.org/10.1016/j.apradiso.2016.10.009). URL: <https://www.sciencedirect.com/science/article/pii/S0969804316302184> (visited on 05/01/2021).
- [58] Xiao Wu et al. “A 20-pW Discontinuous Switched-Capacitor Energy Harvester for Smart Sensor Applications”. In: *IEEE Journal of Solid-State Circuits* 52.4 (Apr. 2017). Conference Name: IEEE Journal of Solid-State Circuits, pp. 972–984. ISSN: 1558-173X. DOI: [10.1109/JSSC.2016.2645741](https://doi.org/10.1109/JSSC.2016.2645741).
- [59] Sha Xue et al. “Methods for improving the power conversion efficiency of nuclear-voltaic batteries”. In: *Nuclear Instruments and Methods in Physics Research Section A: Accelerators, Spectrometers, Detectors and Associated Equipment* 927 (May 21, 2019), pp. 133–139. ISSN: 0168-9002. DOI: [10.1016/j.nima.2019.01.097](https://doi.org/10.1016/j.nima.2019.01.097). URL: <https://www.sciencedirect.com/science/article/pii/S016890021930169X> (visited on 05/20/2021).
- [60] Yang Yang, Xiao-Juan Wei, and Jing Liu. “Suitability of a thermoelectric power generator for implantable medical electronic devices”. In: *Journal of Physics D: Applied Physics* 40.18 (Aug. 30, 2007). Publisher: IOP Publishing, p. 5790. ISSN: 0022-3727. DOI: [10.1088/0022-3727/40/18/042](https://doi.org/10.1088/0022-3727/40/18/042). URL: <https://iopscience.iop.org/article/10.1088/0022-3727/40/18/042/meta> (visited on 04/27/2021).
- [61] Lu Yin et al. “High Performance Printed AgO-Zn Rechargeable Battery for Flexible Electronics”. In: *Joule* 5.1 (Jan. 20, 2021), pp. 228–248. ISSN: 2542-4351. DOI: [10.1016/j.joule.2020.11.008](https://doi.org/10.1016/j.joule.2020.11.008). URL: <https://www.sciencedirect.com/science/article/pii/S254243512030516X> (visited on 04/27/2021).
- [62] *Yttrium oxide, europium doped 756490*. 68585-82-0. URL: <https://www.sigmaaldrich.com/catalog/product/aldrich/756490> (visited on 05/09/2021).

- [63] Zicheng Yuan et al. “High-Performance Micro-Radioisotope Thermoelectric Generator with Large-Scale Integration of Multilayer Annular Arrays through Screen Printing and Stacking Coupling”. In: *Energy Technology* n/a (n/a), p. 2001047. ISSN: 2194-4296. DOI: <https://doi.org/10.1002/ente.202001047>. URL: <https://onlinelibrary.wiley.com/doi/abs/10.1002/ente.202001047> (visited on 04/27/2021).
- [64] *YYG 560 200 isiphoriSUP₂(R)/SUP₂ 900424*. Yellow phosphor. URL: <https://www.sigmaaldrich.com/catalog/product/aldrich/900424> (visited on 05/09/2021).
- [65] A. Zebda et al. “Single Glucose Biofuel Cells Implanted in Rats Power Electronic Devices”. In: *Scientific Reports* 3.1 (Mar. 22, 2013). Number: 1 Publisher: Nature Publishing Group, p. 1516. ISSN: 2045-2322. DOI: [10.1038/srep01516](https://doi.org/10.1038/srep01516). URL: <https://www.nature.com/articles/srep01516> (visited on 04/27/2021).
- [66] Abdelkader Zebda et al. “Challenges for successful implantation of biofuel cells”. In: *Bioelectrochemistry* 124 (Dec. 1, 2018), pp. 57–72. ISSN: 1567-5394. DOI: [10.1016/j.bioelechem.2018.05.011](https://doi.org/10.1016/j.bioelechem.2018.05.011). URL: <https://www.sciencedirect.com/science/article/pii/S1567539417304231> (visited on 04/27/2021).
- [67] Hao Zhang et al. “A flexible and implantable piezoelectric generator harvesting energy from the pulsation of ascending aorta: in vitro and in vivo studies”. In: *Nano Energy* 12 (Mar. 1, 2015), pp. 296–304. ISSN: 2211-2855. DOI: [10.1016/j.nanoen.2014.12.038](https://doi.org/10.1016/j.nanoen.2014.12.038). URL: <https://www.sciencedirect.com/science/article/pii/S2211285514003073> (visited on 04/27/2021).
- [68] *ZPower XR7734 Rechargeable Battery*. URL: https://www.zpowerbattery.com/wp-content/themes/zpower/downloads/ZPower-XR7734_Datasheet.pdf (visited on 04/27/2021).
- [69] Adrian Zurbuchen et al. “Endocardial Energy Harvesting by Electromagnetic Induction”. In: *IEEE Transactions on Biomedical Engineering* 65.2 (Feb. 2018). Conference Name: IEEE Transactions on Biomedical Engineering, pp. 424–430. ISSN: 1558-2531. DOI: [10.1109/TBME.2017.2773568](https://doi.org/10.1109/TBME.2017.2773568).